

1 Local wind regime induced by giant linear dunes:
2 comparison of ERA5-Land ~~re-analysis~~ reanalysis
3 with surface measurements

4 Cyril Gadal · Pauline Delorme ·
5 Clément Narteau · Giles F.S. Wiggs ·
6 Matthew Baddock · Joanna M. Nield ·
7 Philippe Claudin

8
9 Received: DD Month YEAR / Accepted: DD Month YEAR

10 **Abstract**

11 Emergence and growth of sand dunes results from the dynamic interaction be-
12 tween topography, wind flow and sediment transport. While feedbacks between
13 these variables are well studied at the scale of a single and relatively small dune,
14 the average effect of a periodic large-scale dune pattern on atmospheric flows
15 remains poorly constrained, due to a pressing lack of data in major sand seas.
16 Here, we compare field local measurements of surface wind data winds to the
17 predictions of the ERA5-Land climate reanalysis at four locations in Namibia,
18 ~~including within the giant-dune both within and outside the giant linear dune~~
19 field of the Namib ~~sand sea~~Sand Sea. In the desert plains to the north of
20 the sand sea, observations and predictions agree well. This is also the case in
21 the interdune areas of the sand sea, ~~, except for the weak winds blowing at~~
~~night, which exhibit additional components during the day. During the night,~~

C. Gadal

Institut de Mécanique des Fluides de Toulouse, Université de Toulouse Paul Sabatier, CNRS,
Toulouse INP-ENSEEIHT, Toulouse, France. E-mail: cyril.gadal@imft.fr

P. Delorme

Energy and Environment Institute, University of Hull, Hull, UK.

C. Narteau

Institut de Physique du Globe de Paris, Université de Paris, CNRS, Paris, France.

G. Wiggs

School of Geography and the Environment, University of Oxford, Oxford, UK.

M.C. Baddock

Geography and Environment, Loughborough University, Loughborough, UK.

J.M. Nield

School of Geography and Environmental Science, University of Southampton, Southampton,
UK.

P. Claudin

Physique et Mécanique des Milieux Hétérogènes, CNRS, ESPCI Paris, PSL Research Uni-
versity, Université de Paris, Sorbonne Université, Paris, France.

however, an additional wind component aligned with the giant dune orientation, which are not measured, in contrast to the easterly wind predicted by the ERA5-Land reanalysis. We quantify these similarities and differences and provide a physical understanding of the relevant aerodynamical regimes to relate them. For the given dune orientation and measured wind regime, we link the observed wind deviation (over 50°) to the daily cycle of the turbulent atmospheric boundary layer over a dune pattern of given wavelength. We conclude by identifying the conditions under which the ERA5-Land reanalysis data can reliably be used to study dune morphodynamics. We also propose that, in multidirectional wind regimes, deflections of specific winds. During the night, a shallow boundary layer induces a flow confinement above the giant dunes, resulting in large flow deviations, especially for the slower easterly winds. During the day, the feedback of the giant dunes on the atmospheric flow is much weaker due to the thicker boundary layer and higher wind speeds. Finally, we propose that the confinement mechanism and the associated wind deflections induced by giant dunes could explain the occurrence of secondary dune patterns with a different orientation to the primary structures between which they develop. development of smaller-scale secondary dunes, which elongate obliquely in the interdune areas of the primary dune pattern.

Keywords Atmospheric boundary layer · Sand dunes · Flow over hills

43 1 Introduction

44 The description of turbulent flows over complex topography is relevant for a
45 large variety of different environmental systems (Finnigan et al. 2020)(Sherman 1978; Walmsley et al. 1982; Baines 1995;
46 . For example, the flow over hills is of primary interest for wind power, me-
47 teorological and air pollution phenomena (Taylor et al. 1987). The prop-
48 erties of these flows are also key to the understanding of geophysical phe-
49 nomena, including the formation of wind-driven waves on the ocean surface
50 (Sullivan and McWilliams 2010), dissolution bedforms (Claudin et al. 2017)
51 (Claudin et al. 2017; Guérin et al. 2020), or sedimentary ripples and dunes
52 (Charru et al. 2013; Courrech du Pont 2015)(Bagnold 1941; Charru et al. 2013; Courrech du Pont 2015)
53 . Importantly, the troposphere presents a vertical structure, with a lower con-
54 vective boundary layer, of typical kilometer-scale thickness, capped by a stably
55 stratified region (Stull 1988). The largest topographic obstacles, such as moun-
56 tains, can therefore interact with this upper region and lead to internal wave
57 generation or significant wind disturbances, such as lee-side downslope winds
58 (Durran 1990).

59 ~~Focusing on the wind close to the surface, two related~~ Compared to hills and
60 ~~mountains, aeolian sand dunes offer idealized elevation profiles for the study~~ of atmospheric turbulent flow over topographies, due to their smooth shape,
61 ~~free of canopies. Besides, dunes provide a rather wide range of scales, from~~ decameters to kilometers, and very often come in a fairly regular pattern, which
62 ~~further simplifies the flow structure analysis. Past studies have highlighted~~ two important topographic feedbacks on the ~~windflow over dunes can be~~
63 ~~commented on separately~~ wind flow close to the dune/hill surface. First is the
64 effect on wind speed, with documented flow acceleration on upwind slopes
65 (Weaver and Wiggs 2011) and deceleration on downwind slopes (Baddock et al.
66 2007), where the speed-up factor is essentially proportional to the obstacle
67 aspect ratio (Jackson and Hunt 1975). ~~Importantly, the velocity maximum Under~~ Under
68 ~~multidirectional wind regimes with frequent wind reversals, this speed-up effect~~ multidirectional wind regimes with frequent wind reversals, this speed-up effect
69 ~~induces large differences in the amplitude and orientation of the resultant~~ induces large differences in the amplitude and orientation of the resultant
70 sediment transport between flat sand beds and the dune crests (Zhang et al. 2014; Rozier et al. 2019; Gao et al. 2021)
71 . In addition, the position of maximum velocity is typically shifted upwind
72 of the obstacle crest (Jackson and Hunt 1975; Clauvin et al. 2013). This be-
73 haviour has been theoretically predicted by means of asymptotic analysis of a
74 neutrally stratified boundary-layer flow over an obstacle of vanishing aspect ra-
75 ~~tio (Jackson and Hunt 1975; Mason and Sykes 1979; Sykes 1980; Hunt et al. 1988; Belcher and Hunt 1998)~~ (Jackson and Hunt 1975; Mason and Sykes 1979; Sykes 1980; Hunt et al. 1988; Belcher and Hunt 1998; Kroy et al. 2002
76 . Experiments in flumes (Zilker et al. 1977; Zilker and Hanratty 1979; Freder-
77 ick and Hanratty 1988; Poggi et al. 2007; Bristow et al. 2022), in wind tunnels
78 (Gong and Ibbetson 1989; Finnigan et al. 1990; Gong et al. 1996) and in
79 field conditions ~~at all scales~~ (Taylor and Teunissen 1987; Clauvin et al. 2013;
80 Fernando et al. 2019; Lü et al. 2021), have also documented this effect. Inter-
81 estingly, a similar behaviour exists for the pressure perturbation, but with a
82 slight downwind shift for the pressure minimum (Clauvin et al. 2021).

The second effect, much less studied, is the flow deflection that occurs when the incident wind direction is not perpendicular to the ridge crest. While predicted to be small (less than 10°) in the linear regime valid for shallow topography (Gadal et al. 2019), significant flow steering has been reported in the field on the downwind side of steep enough obstacles, such as mountain ranges (Kim et al. 2000; Lewis et al. 2008; Fernando et al. 2019), well-developed sand dunes (Walker et al. 2009; Hesp et al. 2015; Walker et al. 2017; Smith et al. 2017; de Winter et al. 2017; Tsoar and Yaalon 1983; Sweet and Kocurek 1990; Walker and Nickling 2002; Smith et al. 2017) and in particular coastal foredunes (e.g. Hunter et al. 1983; Rasmussen 1989; Walker et al. 2006, 2009; Hesp et al. 2015; V., mountain ranges (Kim et al. 2000; Lewis et al. 2008; Fernando et al. 2019), and valley topographies (Wiggs et al. 2002; Garvey et al. 2005).

For practical reasons, wind measurement Wind measurements over sand dunes has been have been mainly performed over small bedforms, typically a few meters high (corresponding to several tens of meters long) (e.g. Lancaster et al. (1996), McKenna Neuman et al. (1997), Sauermann et al. (2003), Andreotti et al. (2002), Walker and Nickling (2002), Weaver and Wiggs (2011)). Giant dunes (e.g. Mulligan 1988; Hesp et al. 1989; Lancaster et al. 1996). For practical reasons, fewer studies have performed similar measurements on giant dunes (Hayholm and Kocurek 1988), with kilometer-scale wavelengths and heights of tens of meters, are more difficult to investigate although for several reasons they. However, such large dunes provide a choice configuration for the study of turbulent flows over a complex topography. First, one expects larger wind disturbances for larger obstacles. Secondly, their large size makes can make them interact with the vertical structure of the atmosphere (Andreotti et al. 2009). Third, they usually form large patterns in sand seas and thus behave as rather clean periodic perturbations, in contrast with isolated dunes. Finally, because the morphodynamics of aeolian bedforms are is strongly dependent on the local wind regime (Livingstone and Warren 2019), one can expect to see the consequences of windflow disturbance by large dunes on neighbouring small dunes (Brookfield 1977; Ewing et al. 2006). A similar effect is observed on the properties of impact ripple patterns due to the presence of dunes (Howard 1977; Hood et al. 2021)(Howard 1977; Hood et al. 2021).

. Atmospheric flows have been much studied at the desert-scale with climate reanalyses based on global atmospheric models (Blumberg and Greeley 1996; Livingstone et al. 2010; Ashkenazy et al. 2012; Blumberg and Greeley 1996; Livingstone et al. 2010; Ashkenazy et al. 2012; Jolivet et al. 2021; Hu et al. 2021; Gunn et al. 2021), such as ERA-40, ERA-Interim or ERA5 (Uppala et al. 2005; Dee et al. 2011; Hersbach et al. 2020). However, the spatial resolution of these reanalyses (tens of kilometers) of these reanalyses implies average quantities that do not resolve the smaller scales of interest, which range from individual dunes to small mountains (Livingstone et al. 2010). Recently, the release of ERA5-Land has partly resolved this limitation by providing up to 70 years of hourly wind predictions at a 9 km spatial resolution (Muñoz-Sabater et al. 2021). However, its validity remains to be studied, especially in remote desert areas where assimilation of measured data is very low.

In this work, we compare local wind speeds and directions measured by meteorological stations at four different locations inside and north of the

133 ~~giant-dune giant linear dune~~ field of the Namib sand sea to the regional predictions
134 of the ERA5-Land climate reanalysis. Where the meteorological stations
135 are surrounded by a relatively flat environment, we show that local measurements
136 and regional predictions agree well. The agreement is also good in the
137 interdune areas of the sand sea, except for some weak winds blowing at night,
138 which exhibit an additional component aligned with the giant dune orientation.
139 These winds are not predicted by the ERA5-Land reanalysis (section 2 2).
140 Further, we are able to link the magnitude of these differences to the circadian
141 cycle of the atmospheric boundary layer (section 3 3). Finally, we draw
142 implications for the wind disturbances on smaller-scale dunes (section 4 4),
143 suggesting a possible origin for crossing dunes ~~a distinctive secondary dune~~
144 ~~form observed in the Namib and other sand seas.~~

145 2 Wind regimes across the Namib Sand Sea

146 We measured the wind regime at four different locations in Namibia, repre-
147 sentative of various arid environments across the Namib desert (Fig. 1, **Online**
148 **Resource** Fig. 42). The Etosha West station was located at the Adamax wa-
149 terhole to the west of Etosha Pan in northern Namibia, in a sparsely vegetated
150 area. The Huab station was near the coast on a hyper-arid flat gravel plain
151 lying north ~~of~~ the ephemeral Huab river. Here, barchan dunes up to a few me-
152 ters in height develop from the sediment blowing out of the river valley (Nield
153 et al. 2017; Hesp and Hastings 1998). These two stations were both located
154 in relatively flat environments. In contrast, the North Sand Sea and South
155 Sand Sea stations were located in the interdunes between linear dunes with
156 kilometer-scale wavelengths, hectometer-scale heights and superimposed pat-
157 terns. In this section, we describe and compare winds from local measurements
158 and climate reanalysis predictions.

159 2.1 Wind and elevation data

160 At each meteorological station (Fig. 1), wind speed and direction were sam-
161 pled every 10 minutes using cup anemometers (Vector Instruments A100-LK)
162 and wind vanes (Vector Instruments W200-P) at ~~heights which varied a single~~
163 ~~height, which was~~ between 2 m and 3 m depending on the station. The avail-
164 able period of measurements at each station ranged from 1 to 5 discontinuous
165 years distributed between 2012 and 2020 (Online Resource Fig. S24). We
166 checked that at least one complete seasonal cycle was available for each sta-
167 tion. Regional winds were extracted at the same locations and periods from the
168 ERA5-Land dataset, which is a replay at a smaller spatial resolution of ERA5,
169 the latest climate reanalysis from the ~~ECMWWF~~-ECMWF (Hersbach et al.
170 2020; Muñoz-Sabater et al. 2021). This dataset provided hourly predictions
171 of the 10-m wind velocity and direction at a spatial resolution of $0.1^\circ \times 0.1^\circ$
172 ($\simeq 9$ km in Namibia).

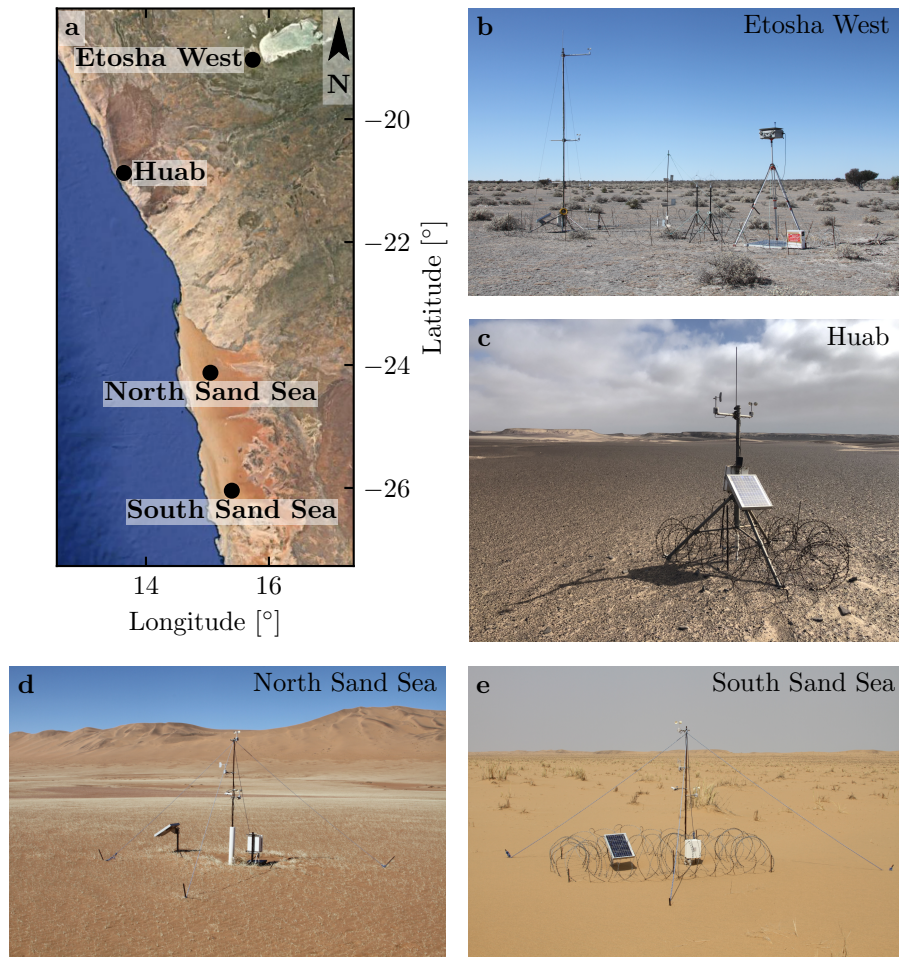


Fig. 1 Wind data used in this study Studied field sites. **a:** Location of the different sites in Namibia. **b–e:** Satellite images Photographs of these different environments (Google-Earth, Maxar Technologies, CNES/Airbus). In each subplot, the left and right wind roses represent the data from the ERA5-Land climate reanalysis and the local wind stations, respectively. Note that the bars show the direction towards which the wind blows. The black dots show the location of local wind meteorological stations.

To enable direct comparison, the local wind measurements were averaged into 1-hr bins centered on the temporal scale of the ERA5-Land estimates (Online Resource Fig. S3S2). As the wind velocities of both datasets were provided at different heights, we converted them into shear velocities u_* (Online Resource section 1), characteristic of the turbulent wind profile. Wind roses in Fig. 1(b–e) show the resulting wind data.

Dune properties were computed using autocorrelation on the 30-m Digital Elevation Models (DEMs) of the shuttle radar topography mission (Farr et al.

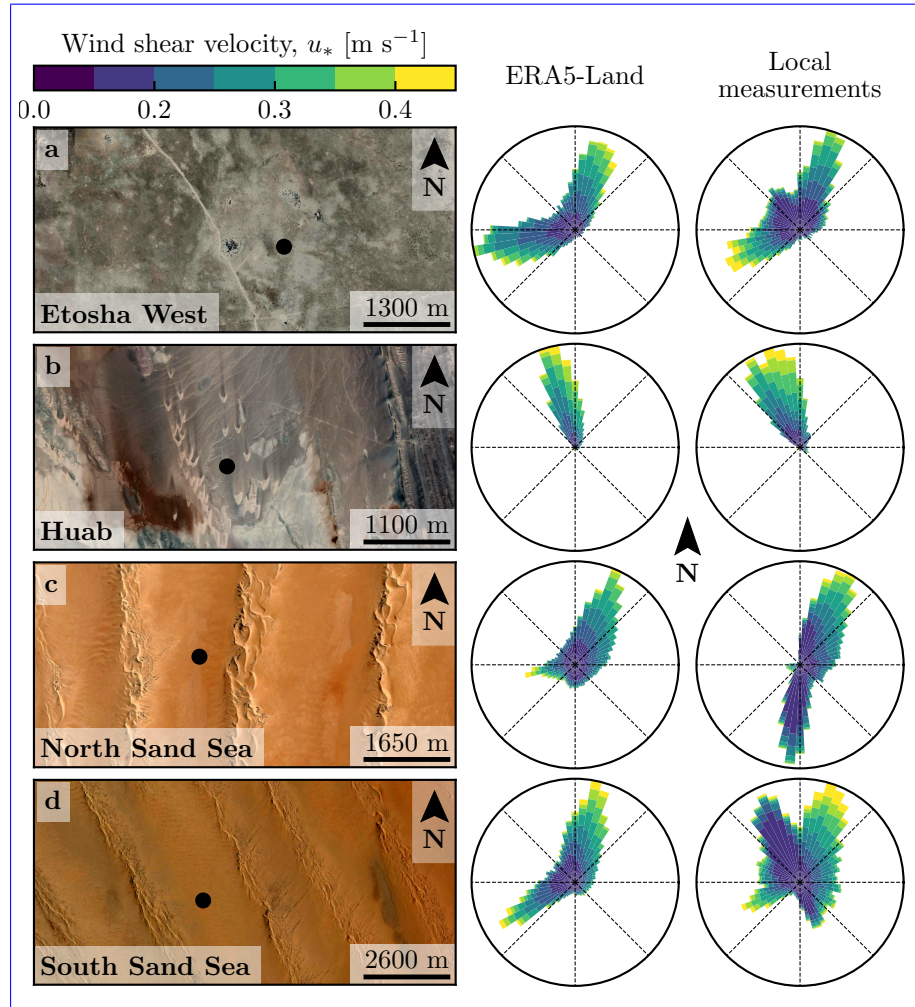


Fig. 2 Wind data used in this study. Satellite images of the different environments (Google-Earth, Maxar Technologies, CNES/Airbus) are shown on the left. The black dots show the location of the wind measurements stations. On the right of the photos, the corresponding wind roses representing the data from the ERA5-Land climate reanalysis and the local wind stations are displayed. Note: the graphical convention for the wind roses is that the bars show the direction towards which the wind blows (see color bar for velocity scale).

181 2007). For the North and South Sand Sea stations, we obtain, respectively,
 182 orientations of 85° and 125° with respect to the North, wavelengths of 2.6 km
 183 and 2.3 km and amplitudes (or half-heights) of 45 m and 20 m (Online Resource
 184 Fig. S5–S4 for more details). This agrees with direct measurements made on
 185 site.

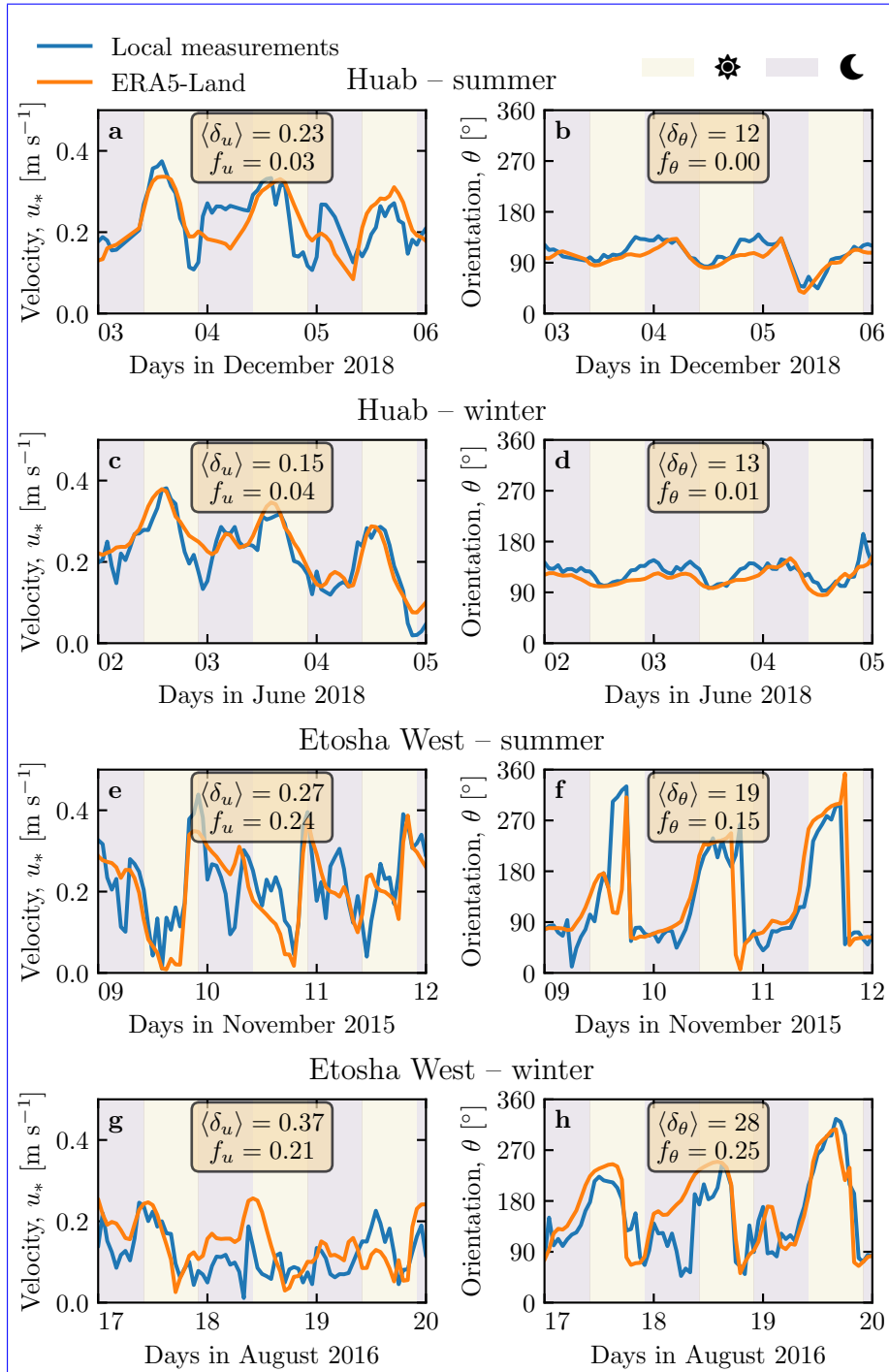


Fig. 3 Temporal comparison between the wind data coming from the ERA5-Land climate reanalysis (orange lines) and from the local measurements (blue lines). Coloured swathes indicate day (between 1000–10.00 UTC and 2200–22.00 UTC) and night (before 1000–10.00 UTC or after 2200–22.00 UTC). Numbers in legends indicate the average flow deflection δ_θ and relative wind modulation δ_u over the displayed period (see section 3.2 for their definitions), as well as the percentage f_θ and f_u of occurrence of extreme events ($\delta_\theta > 50^\circ$, $|\delta_u| > 0.6$). **a–b:** Etosha West–Huab station in summer. **b–c:** Etosha West–Huab station in winter. **d–e:** North–Sand–Sea–Etosha West station in summer. **f–g:** North–Sand–Sea–Etosha West station in winter. Time series of the two other stations are shown in Online Resource Fig. S65.

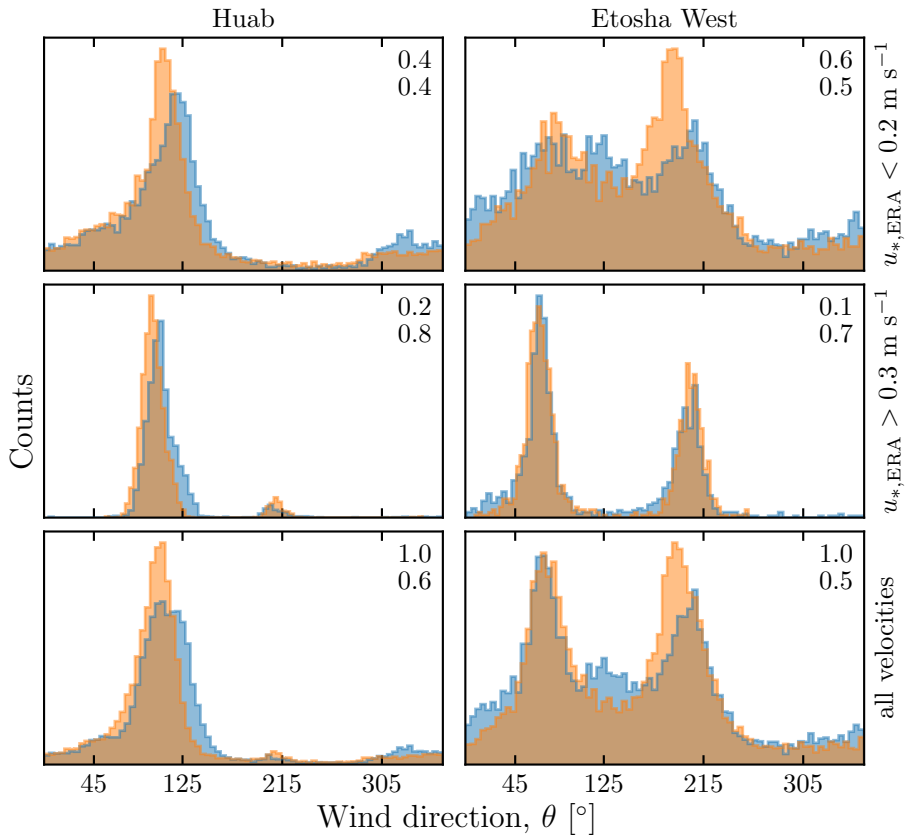


Fig. 4 Distributions of wind direction at Huab and Etosha West stations for the ERA5-Land climate reanalysis (orange) and the local measurements (blue). In each subplot, both distributions are plotted from the same time steps, selected for different ranges of the wind wind velocity (rows) in the ERA5-Land dataset. The numbers at the upper right corners give the percentage of time steps selected in each sub-range (top), as well as the percentage of them corresponding to the day – defined between 10.00 UTC and 22.00 UTC (bottom).

186 2.2 Comparison of local and regional winds

187 The measured and predicted wind regimes are shown in Fig. 12. In the Namib,
 188 the regional wind patterns are essentially controlled by the sea breeze, resulting
 189 in strong northward components (sometimes slightly deviated by the large
 190 scale topography) present in all regional wind roses (Lancaster 1985). These
 191 daytime winds are dominant during the period October–March (Fig. 23f and
 192 Online Resource Fig. S64f). During April–September, an additional (and often
 193 nocturnal) easterly component can also be recorded, induced by the combination
 194 of katabatic winds forming in the mountains, and infrequent ‘berg’ winds,
 195 which are responsible for the high wind velocities observed (Lancaster et al.
 196 1984). The frequency of these easterly components decreases from inland to the
 197 coast. As a result, bidirectional wind regimes within the Namib Sand Sea and

at the west Etosha site (Fig. 1b,d,e~~2a,c,d~~) and a unidirectional wind regime on the coast at the outlet of the Huab River (Fig. 4e~~2b~~) are observed.

In the case of the Etosha West and Huab stations, the time series of wind speed and direction from the regional predictions quantitatively match those corresponding to the local measurements (Fig. 2a-d) Figs. 3, 4 and Online Resource Figs. S6a-d, S7, S9 Fig. S5). For the North Sand Sea and South Sand Sea stations within the giant linear dune field, we observe that this agreement is also good, but limited to the October-March time period (Fig. 2e-h and and Online Resource Fig. S6e-h~~4a, b, e, f~~). However, the field-measured wind roses exhibit additional wind components aligned with the giant dune orientation, as evidenced on the satellite images (Fig. 42c,d).

More precisely, during the April-September period, the local and regional winds in the interdune match during daytime only, i.e. when the southerly/-southwesterly sea breeze dominates (Figs. 2e,f and 3, Online Resource Fig. S8~~5c,d,g,h and 6~~). In the late afternoon and during the night, when the easterly ‘berg’ and katabatic winds blow, measurements and predictions differ. In this case, the angular wind distribution of the local measurements exhibits two additional modes corresponding to reversing winds aligned with the giant dune orientation (purple frame in Fig. 36, Online Resource Figs. S8 and S10 Fig. S6). This deviation is also associated with a general attenuation of the wind strength (Online Resource Fig. S14S7). Remarkably, all these figures show that these wind reorientation and attenuation processes occur only at low velocities of the regional wind, typically for $u_{*, ERA} \lesssim 0.2 \text{ m s}^{-1}$ $u_{*, ERA5-Land} \lesssim 0.2 \text{ m s}^{-1}$. For shear velocities larger than $u_{*, ERA} \approx 0.3 \text{ m s}^{-1}$ $u_{*, ERA5-Land} \approx 0.3 \text{ m s}^{-1}$, the wind reorientation is not apparent. Finally, for intermediate shear velocities, both situations of wind flow reoriented along the dune crest and not reoriented can be successively observed (Online Resource Fig. S10S6). Importantly, these values are not precise thresholds (~~and certainly not related to the threshold for sediment transport~~), but indicative of a crossover between regimes, whose physical interpretation is discussed in the next section.

3 Influence of wind speed and circadian cycle on the atmospheric boundary layer

The wind deflection induced by linear dunes has previously been related to the incident angle between wind direction and crest orientation, with a maximum deflection evident for incident angles between 30° and 70° (Walker et al. 2009; Hesp et al. 2015). In the data analysed here, the most deflected wind at both the North and South Sand Sea stations is seen to be where the incident angle is perpendicular to the giant dunes (Figs. 4 and 3, Online Resource Fig. S8~~2 and 6~~). It therefore appears that in our case, the incident wind angle is not the dominant control on maximum wind deflection. Further, and as shown in Fig. 36, winds of high and low velocities show contrasting behaviour in characteristics of deflection. This suggests a change in hydrodynamical regime between the winds. In this section, we discuss the relevant parameters associ-

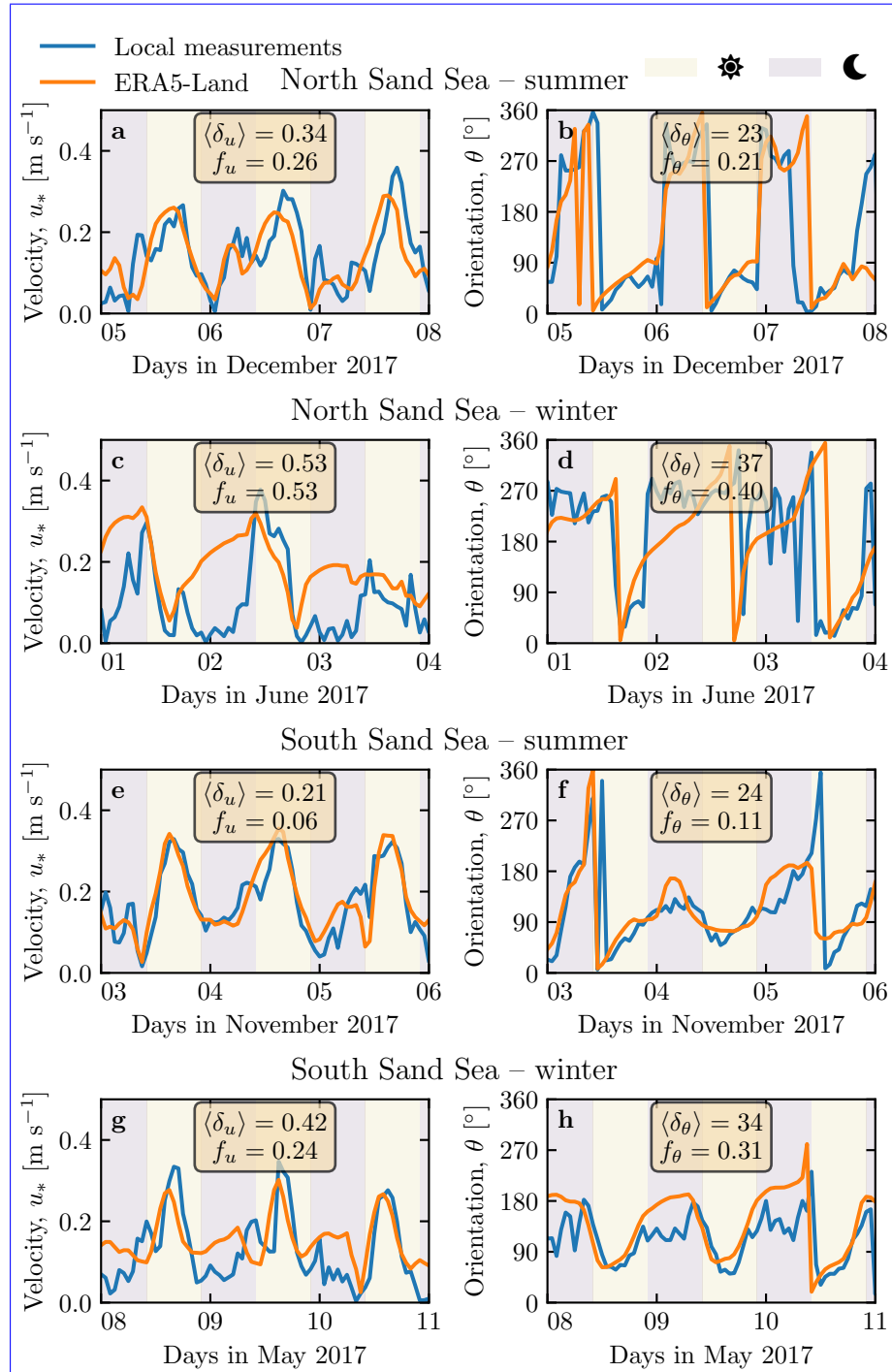


Fig. 5 Distributions of wind direction at the Same as Fig. 3 for North Sand Sea Station for the ERA5 Land climate reanalysis (orange) and the local measurements station in summer (bluea–b). In each subplot, both distributions are plotted from the same time steps; selected with constraints on the wind direction (columns) and/or wind velocity (rows) of the ERA5 Land dataset. The grey vertical dashed lines indicate the dune orientation. The numbers at the top right give the percentage of time steps selected North Sand Sea station in each sub-range, as well as the percentage corresponding to the daytime winter (between 1000 UTC and 2200 UTCb–c). The purple frame highlights the regime (low wind velocities, nocturnal easterly wind) South Sand Sea station in which the data from both datasets differ. A similar figure can be obtained for the North summer (d–e) and South Sand Sea station in winter (Online Resource Fig. S8f–g).

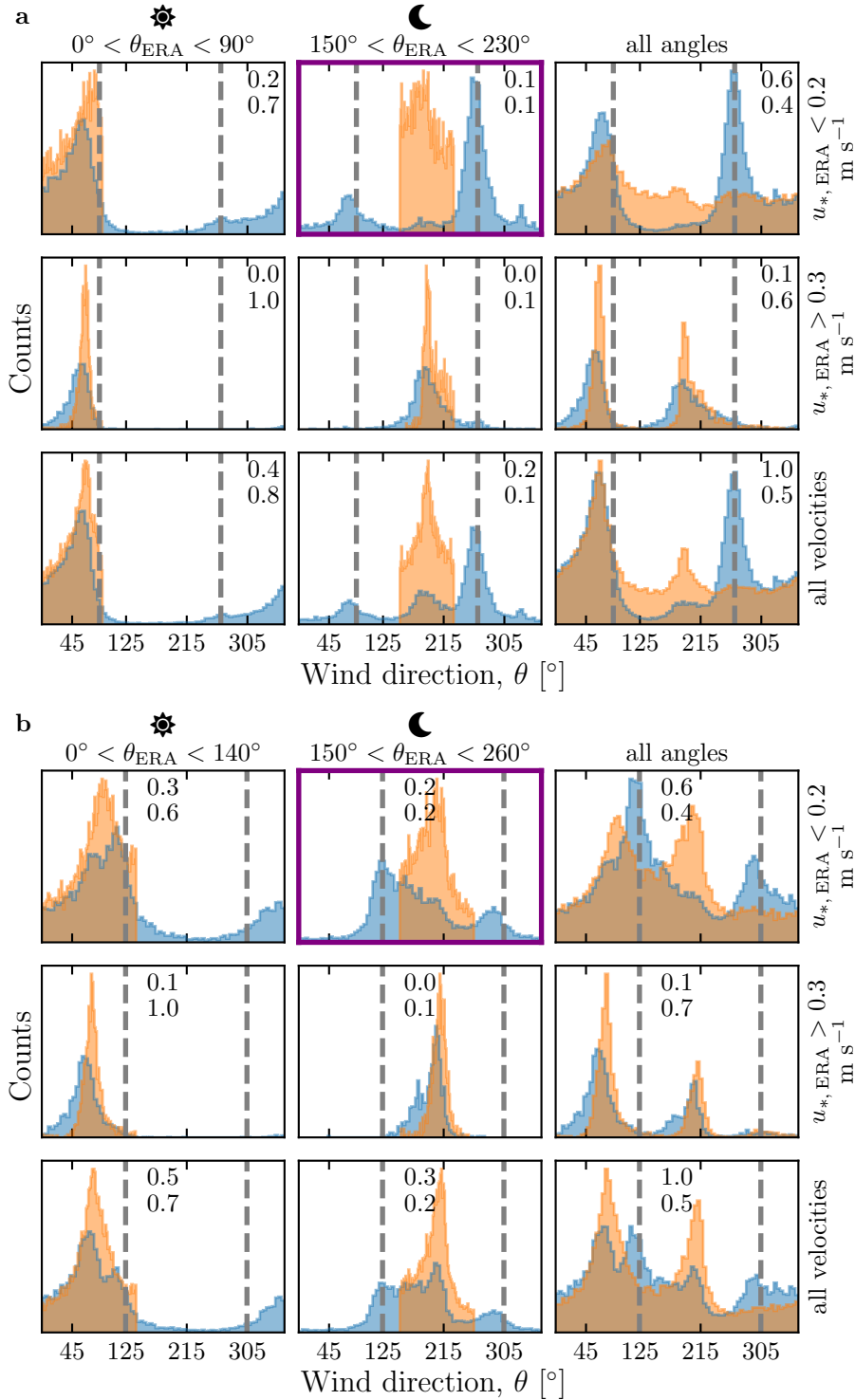


Fig. 6 Same as Fig. 4 but for North Sand Sea (a) and South Sand Sea (b) stations. Here, subplots correspond to different ranges for the wind direction (columns) and wind velocity (rows) of the ERA5-Land dataset. The grey vertical dashed lines indicate the main dune orientation. In contrast with observations at the Huab and Etosha West stations (Fig. 4), histograms do not match well at low wind velocities, and the purple frame highlights the regime (low wind velocities, nocturnal easterly wind) in which the data from both datasets differ most.

241 ated with the dynamical mechanisms that govern the interactions between the
242 atmospheric boundary layer flow and giant dune topographies. This analysis
243 allows us to provide a physics-based interpretation of our measured wind data.

244 3.1 Flow over a modulated bed

245 Taking as a reference the turbulent flow over a flat bed, the general framework
246 of our study is understanding and describing the flow response to a bed mod-
247 ulation (e.g. a giant dune). Without loss of generality, we can consider in this
248 context an idealised bed elevation in the form of parallel sinusoidal ridges, with
249 wavelength λ (or wavenumber $k = 2\pi/\lambda$) and amplitude ξ_0 , and where the ref-
250 erence flow direction makes a given incident angle with respect to the ridge
251 crest (Andreotti et al. 2012). Part of this response, on which we focus here,
252 is the flow deflection by the ridges. In a simplified way, it can be understood
253 from the Bernoulli principle (Hesp et al. 2015): as the flow approaches the
254 ridge crest, the compression of the streamlines results in larger flow velocities,
255 and thus lower pressures ([Rubin and Hunter 1987](#)) ([Jackson and Hunt 1975](#)).
256 An incident flow oblique to the ridge is then deflected towards lower pressure
257 zones, i.e towards the crest. Turbulent dissipation tends to increase this effect
258 downstream, resulting in wind deflection along the crest in the lee side (Gadal
259 et al. 2019).

260 Flow confinement below a capping surface, which enhances streamline com-
261 pression, has a strong effect on the hydrodynamic response and typically in-
262 creases flow deflection. This is the case for bedforms forming in open channel
263 flows such as rivers ([Fourrière et al. 2010; Unsworth et al. 2018](#)) ([Kennedy 1963](#); [Chang and Simons 1970](#); [Mizumura 1995](#)).
264 . This is also relevant for aeolian dunes as they evolve in the turbulent atmo-
265 spheric boundary layer (ABL) capped by the stratified free atmosphere (FA)
266 (Andreotti et al. 2009). Two main mechanisms, associated with dimensionless
267 numbers must then be considered (Fig. 47). First, topographic obstacles typi-
268 cally disturb the flow over a characteristic height similar to their length. As
269 flow confinement is characterised by a thickness H , the interaction between
270 the dunes and the wind in the ABL is well captured by the parameter kH .
271 The height H is directly related to the [radiative fluxes at sensitive heat flux](#)
272 [from](#) the Earth surface. It is typically on the order of a kilometre, but sig-
273 nificantly varies with the circadian and seasonal cycles. Emerging and small
274 dunes, with wavelengths in the range 20 to 100 m, are not affected by the
275 [flow](#) confinement, corresponding to $kH \gg 1$. For giant dunes with [kilometric](#)
276 [kilometer-scale](#) wavelengths, however, their interaction with the FA [is-can be](#)
277 significant (Andreotti et al. 2009). This translates into a parameter kH in the
278 range 0.02–5, depending on the moment of the day and the season. A second
279 important mechanism is associated with the existence of a thin intermediate
280 so-called capping layer between the ABL and the FA. It is characterised by a
281 density jump $\Delta\rho$, which controls the ‘rigidity’ of this interface, i.e. how much
282 its deformation affects streamline compression. This is usually quantified using
283 the Froude number (Vosper 2004; Stull 2006; Sheridan and Vosper 2006; Hunt

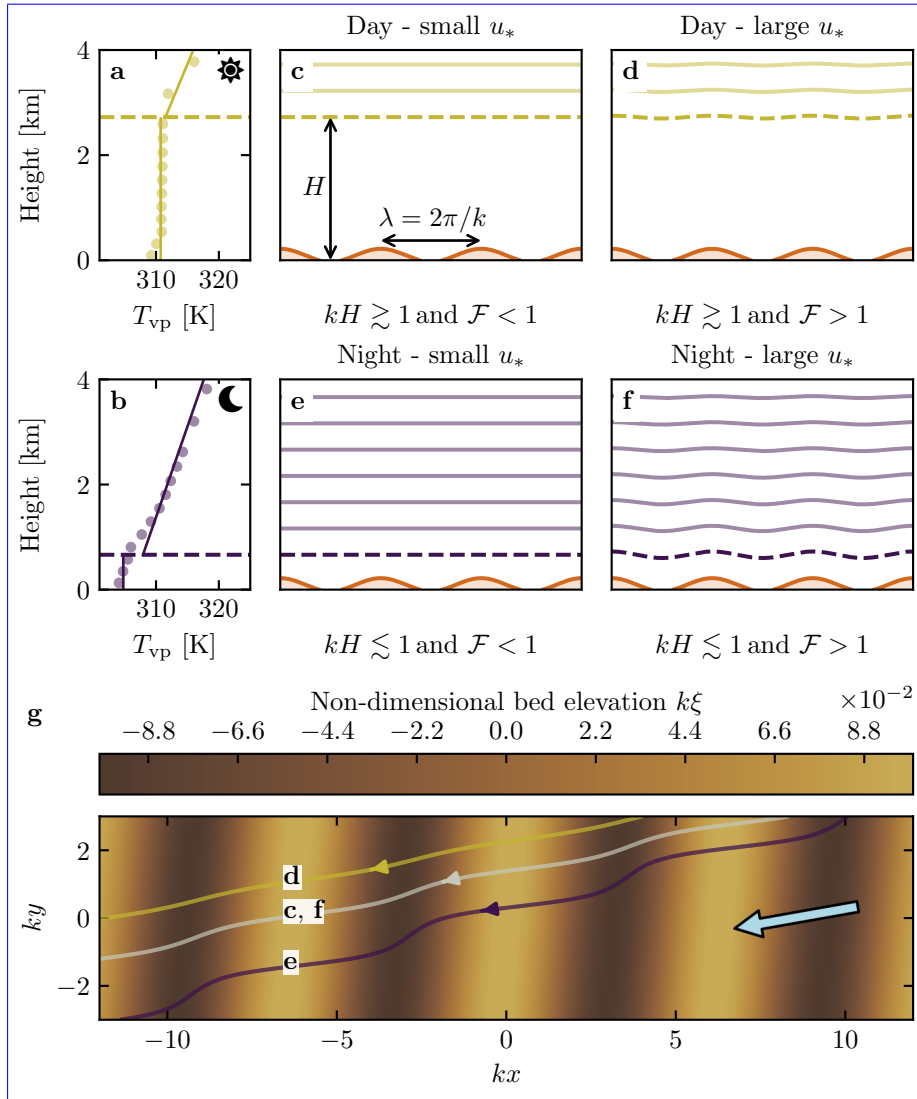


Fig. 7 **a–b:** Vertical profiles of the virtual potential temperature T_{vp} at **two** different time steps (day - 03/11/2015 - **1200–12.00** UTC, night - 01/13/2013 - **0900–09.00** UTC) at the North Sand Sea station. Dots: data from the ERA5 reanalysis. Dashed lines: boundary layer height given by the ERA5 reanalysis (Online Resource section 2). Plain lines: vertical (boundary layer) and linear (free atmosphere) fits to estimate the stratification properties. **c–f:** Sketches representing the interaction between the giant dunes and the atmospheric flow for different meteorological conditions. **g:** Streamlines over a sinusoidal topography $\xi(x, y)$ qualitatively representing the effect of low, medium and strong flow confinement, in relation to the above panels (see Appendix **4** for more details). The blue arrow indicates the undisturbed wind direction.

²⁸⁴ et al. 2006; Jiang 2014):

$$\mathcal{F} = \frac{U}{\sqrt{\frac{\Delta\rho}{\rho_0} g H}}, \quad (1)$$

²⁸⁵ where U is the wind velocity at the top of the ABL and ρ_0 its average density.
²⁸⁶ The intensity of the stratification, i.e. the amplitude of the gradient $|\partial_z \rho|$
²⁸⁷ in the FA, also impacts its-the ability to deform the capping layer under
²⁸⁸ the presence of an underlying obstacle, and thus affects the influence of flow
²⁸⁹ confinement. This can be quantified using the internal Froude number (Vosper
²⁹⁰ 2004; Stull 2006; Sheridan and Vosper 2006; Hunt et al. 2006; Jiang 2014)
²⁹¹ $\mathcal{F}_I = kU/N$, where $N = \sqrt{-g\partial_z \rho/\rho_0}$ is the Brunt-Väisälä frequency (Stull
²⁹² 1988). Both Froude numbers have in practice the same qualitative effect on
²⁹³ flow confinement (a smaller Froude corresponding to a stiffer interface), and
²⁹⁴ we shall restrict the main discussion to \mathcal{F} only.

²⁹⁵ With this theoretical framework in mind, and in the context of the mea-
²⁹⁶ sured wind data in the North and South Sand Sea stations, the smallest wind
²⁹⁷ disturbances are expected to occur during the day, when the ABL depth is the
²⁹⁸ largest and comparable to the dune wavelength ($kH \gtrsim 1$), which corresponds
²⁹⁹ to a weak confinement situation (Fig. 47c,d). In contrast, large wind dis-
³⁰⁰ turbances are expected to occur during the night, when the confinement is mainly
³⁰¹ induced by a shallow ABL (Fig. 47e). However, this strong confinement can be
³⁰² somewhat reduced in the case of strong winds, corresponding to large values of
³⁰³ the Froude number and a less ‘rigid’ interface (Fig. 47f). This is in qualitative
³⁰⁴ agreement with the transition from deflected to non-deflected winds related to
³⁰⁵ low and high velocities observed in our data (Sec. 2.2).

³⁰⁶ 3.2 Data distribution in the flow regimes

³⁰⁷ We can go one step further and analyse how our data quantitatively spread
³⁰⁸ over the different regimes discussed above. For that purpose, one needs to
³⁰⁹ compute kH and \mathcal{F} from the time series. H , U and the other atmospheric
³¹⁰ parameters can be deduced from the various vertical profiles (temperature,
³¹¹ humidity) available in the ERA5 climate reanalysis (Online Resource section
³¹² 2). We quantify the flow deflection δ_θ as the minimal angle between the wind
³¹³ orientations comparing the local measurements and the regional predictions.
³¹⁴ We also compute the relative velocity modulation as

$$\delta_u = \frac{u_*^{\text{ERA}} - u_*^{\text{station}}}{u_*^{\text{ERA}}} \frac{u_*^{\text{ERA5-Land}} - u_*^{\text{Local mes.}}}{u_*^{\text{ERA5-Land}}}. \quad (2)$$

³¹⁵ These two quantities are represented as maps in the plane (\mathcal{F} , kH) (Fig. 58a,b),
³¹⁶ and one can clearly identify different regions in these graphsplots. Small wind
³¹⁷ disturbances (small δ_θ and δ_u) are located in the top-right part of the diagrams,
³¹⁸ corresponding to a regime with low-interaction as well as low-confinement (kH
³¹⁹ and \mathcal{F} large enough, Fig. 47d). Lower values of kH (stronger interaction) or of

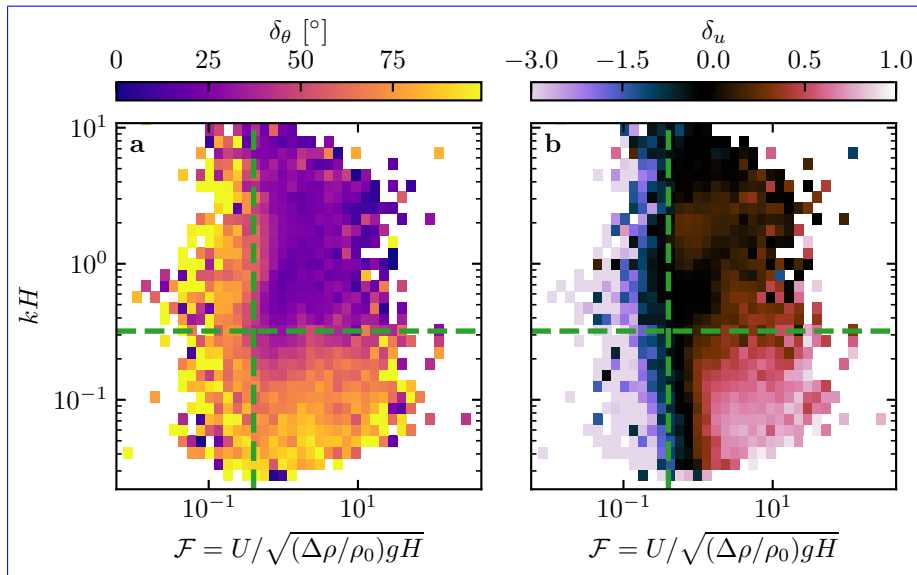


Fig. 8 Regime diagrams of the wind deviation δ_θ (a) and relative attenuation/amplification δ_u (b) in the space (\mathcal{F}, kH) , containing the data from both the North Sand Sea and South Sand Sea stations. **Green** The green dashed lines empirically delimit the different regimes. The point density in each bin of the diagrams is shown in Online Resource Fig. S14–S10 – 95% of the data occur in the range $-1 < \delta u < 1$. Similar regime diagrams in the spaces (\mathcal{F}_I, kH) and $(\mathcal{F}_I, \mathcal{F})$ are shown in Online Resource Fig. S12–S11.

320 Froude number (stronger confinement) both lead to an increase in wind dis-
 321 turbances, both in terms of orientation and velocity. Below a crossover value
 322 $kH \simeq 0.3$, wind disturbance is less sensitive to the \mathcal{F} -value. This is probably
 323 due to enhanced non-linear effects linked to flow modulation by the obstacle
 324 when confinement is strong (e.g. wakes and flow recirculations). The Froude
 325 number also controls a transition from damped to amplified wind velocities
 326 in the interdune, with a crossover around $\mathcal{F} \simeq 0.4$ (Fig. 58b). Such an ampli-
 327 fication is rather unexpected. Checking the occurrence of the corresponding
 328 data, it appears that these amplifications are associated with the southerly
 329 sea breeze, and occur dominantly during the October–March period, when the
 330 other easterly wind is not present (Online Resource Fig. S12a–b). Further-
 331 more, they occur less frequently during the afternoon, and more frequently at
 332 the end of the day (Online Resource Fig. S12c). This effect may be linked
 333 to a change in the flow behaviour in the lee side of the obstacles but further
 334 measurements are needed in order to assess the different possibilities (Baines
 335 1995; Vosper 2004).

336 As the hydrodynamic roughness z_0 determine the magnitude of wind shear
 337 velocities, Froude number \mathcal{F} and relative velocity modulation δ_u , it is important
 338 to discuss the sensitivity of the results to the z_0 -values chosen for both the
 339 ERA5-Land and the field data (see Online Resource section 4). Other quantities
 340 associated with wind direction are independent of this choice. Considering

341 the possible range of realistic roughness values, the uncertainty on velocities
 342 estimated using the law of the wall is at most 30 %. A similar maximum
 343 uncertainty applies to the Froude number. This uncertainty also propagates to
 344 δ_u , for which Figure S14 shows that the choice of roughness has little influence
 345 on its temporal variations even if it can induce a global increase or decrease
 346 of its values. Hence, the choice of the z_0 -values will not qualitatively affect
 347 the overall aspect of the regime diagram presented in Figure 8b. It may only
 348 change the value of δ_u for which the transition between regimes is observed
 349 (dashed green lines in Figure 8b). Our conclusions are thus robust with respect
 350 to the somewhat arbitrary choice of the hydrodynamic roughness values.

351 4 Discussion and conclusion

352 The feedback of the giant dunes on the wind flow has important implications
 353 for smaller ~~seales~~^{scale} bedforms. As illustrated in Fig. 69, small linear dunes
 354 (~ 50 m wide) are often present ~~in~~^{within} the 1–2 km interdune ~~spaces~~^{spaces} be-
 355 tween giant linear dunes in the Namib Sand Sea (Livingstone et al. 2010).
 356 These smaller dunes do not exhibit the same orientation as the large ones,
 357 and are sometimes named ‘crossing dunes’ (Chandler et al. 2022). Whilst dif-
 358 ferences between large and small scale dune patterns are observed ubiqui-
 359 tously, they are ~~largely~~^{usually} attributed to the presence of two different
 360 dune growth mechanisms, leading to two different dune patterns (orientations
 361 and/or morphologies) for the same wind regime (Courrech du Pont et al. 2014;
 362 Runyon et al. 2017; Lü et al. 2017; Song et al. 2019; Gadal et al. 2020; Hu
 363 et al. 2021). Here, however, our arguments enable the development of dif-
 364 fering orientations for the small and giant linear dunes ~~whilst also imposing~~
 365 ~~governed by~~ the same dune growth mechanism (elongating mode). Figure 6
 366 9 shows how the orientations for the small and giant dunes can be derived
 367 from the locally measured and regionally predicted winds respectively (red ar-
 368 rows in Fig. 69). These predictions require ~~a specification for~~ the threshold of
 369 ~~aeolian sand transport~~^{aeolian sand transport} to be specified. Importantly, its
 370 value ~~expressed as~~<sup>(a shear velocity $u_{th} \approx 0.15 \text{ ms}^{-1}$ is reached in the deflected
 371 ~~wind regime already estimated at $u_{th} \approx 0.15 \text{ m s}^{-1}$ – see Appendix 4)~~^{can be}
 372 ~~reached in periods during which deflected winds are observed (recall that the~~^{reached in periods during which deflected winds are observed (recall that the}
 373 ~~stronger winds, responsible for most of the sediment transport and associated~~^{stronger winds, responsible for most of the sediment transport and associated}
 374 ~~dune morphodynamics, are not deflected – see Fig. 6)~~^{dune morphodynamics, are not deflected – see Fig. 6)}. The feedback of the
 375 giant dunes on the wind described in this study, through wind deflection and
 376 attenuation, thus provides a potential explanation for the existence of these
 377 small linear dunes elongating across the interdune, a dynamic which has re-
 378 mained unresolved to date. These crossing dunes could provide additional
 379 constraints for the inference of local winds from bedforms, similarly to that
 380 currently performed on Mars using ripple orientations (Liu and Zimbelman
 381 2015; Hood et al. 2021). Further work is needed to investigate these processes
 382 in more detail, including measurements of sediment transport and flow on the
 383 top of dunes.</sup>

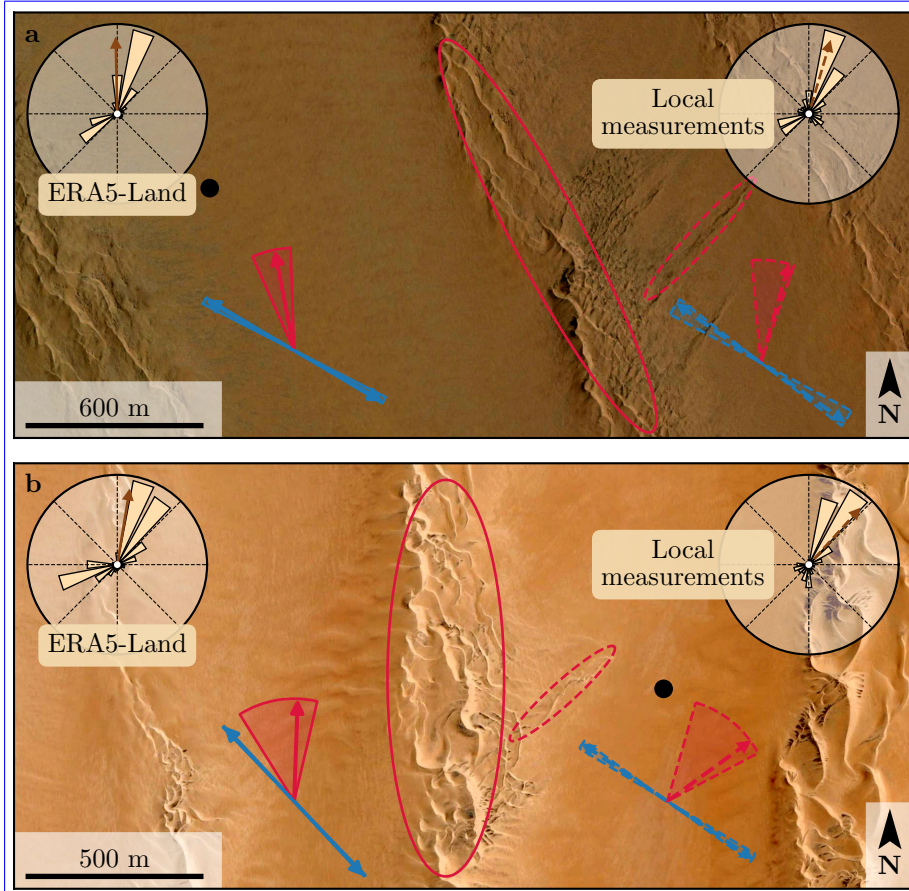


Fig. 9 Implications for smaller scale patterns in (a) the South Sand Sea and (b) North Sand Sea. The ellipses indicate the different types of elongating dunes, at large (plain line) and small (dashed line) scales. Dune orientation are predicted using the model of Courrech du Pont et al. (2014) from the sand flux angular distributions, shown here (roses and along with the resultant transport direction (brown arrow) for typical values (grain size $180 \mu\text{m}$, flux-up ratio of 1.6). Code for corresponding arrows: use of ERA5-Land data (plain line), use of local measurements (dashed line), prediction for the bed instability growth mechanism (blue), prediction for the elongation growth mechanism (red). Wedges show the uncertainty on the orientation calculation when parameters are varied. The black dots indicate the location of the meteorological stations with respect to in the dunes interdune. See Appendix 2–4 for additional details.

This study presents the field and reanalysis-based evidence that wind flow patterns around giant dunes are influenced by the atmospheric boundary layer, particularly during nocturnal conditions. It leaves However, we do not address here the question of the limitation of the giant dune pattern coarsening, and leave open the debate as to whether the size of giant dunes is limited their size is controlled by the depth of this layer (Andreotti et al. 2009), in contrast

390 to ~~an unconstrained dune growth, sediment supply limited and~~ ever-slower
391 ~~with size (?)~~ growth with size (Werner and Kocurek 1999; Gunn et al. 2022).
392 More field evidence is ~~definitively~~ needed from additional dune fields, but this
393 mechanism would ~~then~~ allow for the inference of the ABL depth from giant
394 bedform wavelengths where measurements are not feasible or available, such
395 as Titan (Lorenz et al. 2010).

396 To conclude on conditions under which the ERA5-Land reanalysis data can
397 reliably be used to study dune morphodynamics, we summarise the compari-
398 son of local (direct measurements) and regional (climate reanalysis) wind data
399 ~~as follows~~. In flat areas, the agreement between the two confirms the ability of
400 the ERA5-Land climate reanalysis to predict the wind regime down to scales
401 ~ 10 km, i.e. the model grid. When smaller scale topographies are present
402 (giant dunes in our case), locally measured winds can significantly differ from
403 the regionally predicted ones. This is the case when the disturbances induced
404 by the dunes interact with the lower part of the ABL vertical structure, which
405 presents circadian variations. During the day, when the capping layer is typi-
406 cally high, this interaction is small, and the ERA5-Land predictions are also
407 quantitatively consistent with the local data. During the night, however, the
408 presence of a shallow atmospheric boundary layer induces a strong confine-
409 ment of the flow, and is associated with large wind deflection by the dunes.
410 Importantly, we find that this effect can be counterbalanced for large wind
411 velocities, which are capable of deforming the capping layer, thus decreasing
412 the influence of the confinement.

413 The theoretical computation of the wind disturbances induced by sinu-
414 soidal ridges under flow confinement has been performed in the linear limit
415 (Andreotti et al. 2009, 2012), i.e. when the aspect ~~ration~~^{ratio} of these ridges
416 is small ($k\xi_0 \ll 1$). These models are able to qualitatively reproduce the ob-
417 served wind deflection (Appendix 4, Online Resource Figs. ?? and ??S11 and
418 S13), and thus provide the physical support for the interpretation we propose
419 here based on hydrodynamic regimes. However, these models cannot quanti-
420 tatively predict the magnitude of ~~these~~^{our} observations, probably due to the
421 presence of expected non-linearities in high confinement situations linked to
422 strong flow modulations. Besides, these linear calculations only predict wind
423 attenuation in the interdune, in contrast with the observed enhanced veloc-
424 ities associated with particular evening winds from the ~~South~~^{south} during
425 the period October–March (Online Resource Fig. ??S12). Some other models
426 predict different spatial flow structures in response to a modulated topogra-
427 phy, such as lee waves and rotors (Baines 1995; Vosper 2004). However, our
428 measurements are located at a single point in the interdune, ~~so we are and we~~
429 ~~are thus~~ unable to explore these types of responses. Data at different places
430 along and across the ridges are needed to investigate and possibly map such
431 flow structures, and for further comparisons with the models.

432 **Acknowledgements** We would like to acknowledge the contributors of the following open-
433 source python libraries, Matplotlib (Hunter 2007), Numpy (Harris et al. 2020) and Scipy

434 (Virtanen et al. 2020), which provide an incredibly efficient ecosystem allowing scientific
 435 research in Python. We also thank B. Andreotti and A. Gunn for useful discussions.

436 **Data Availability** All data used in this study can be found in Gadal et al. (2022). Note that
 437 it contains modified Copernicus Climate Change Service Information (2021). Neither the Eu-
 438 ropean Commission nor ECMWF is responsible for any use that may be made of the Coperni-
 439 cus Information or Data it contains. Fully documented codes used Documented codes used in
 440 this study to analyse this study data are available at <https://github.com/Cgadal/GiantDunes>
 441 (will be made public upon acceptance of this manuscript for publication).

442 **Fundings** Multiple grants have supported the collection of wind data through visits to the
 443 four sites between 2013 and 2020 (John Fell Oxford University Press (OUP) Research Fund
 444 (121/474); National Geographic (CP-029R-17); Natural Environment Research Council UK
 445 (NE/R010196/1 and NE/H021841/1 NSFGEO-NERC); Southampton Marine and Maritime
 446 Institute SMMI EPSRC-GCRF UK), along with research permits (1978/2014, 2140/2016,
 447 2304/2017, 2308/2017, RPIV00022018, RPIV0052018, RPIV00230218). The authors are
 448 very grateful for support from Etosha National Park (especially Shyane KöttingKötting,
 449 Boas Erckie, Pierre du Preez, Claudine Cloete, Immanuel Kapofi, Wilferd Versfeld, and
 450 Werner Kilian), Gobabeb Namib Research Institute (Gillian Maggs-KöllingMaggs-Kölling
 451 and Eugene Marais), The Skeleton Coast National Park (Joshua Kazeurua). Various re-
 452 searchers and desert enthusiasts have assisted with instruments and the logistics of expedi-
 453 tions, especially Mary Seely for expert guidance at the North Sand Sea site.

454 Finally, we acknowledge financial support from the Laboratoire d'Excellence UnivEarthS
 455 Grant ANR-10-LABX-0023, the Initiative d'Excellence Université Excellence Université de
 456 Paris Grant ANR-18-IDEX-0001, the French National Research Agency Grants ANR-17-
 457 CE01-0014/SONO and the National Science Center of Poland Grant 2016/23/B/ST10/01700.

458 **Conflict of interest** All authors declare that they have no conflicts of interest.

459 Appendix 1: Linear theory of wind response to topographic pertur- 460 bation

461 Following the work of Fourrière et al. (2010), Andreotti et al. (2012) and
 462 Andreotti et al. (2009), we briefly describe in this appendix the framework
 463 for the linear response of a turbulent flow to a topographic perturbation of
 464 small aspect ratio. As a general bed elevation can be decomposed into Fourier
 465 modes, we focus here on a sinusoidal topography:

$$\xi = \xi_0 \cos [k (\cos(\alpha)y - \sin(\alpha)x)], \quad (3)$$

466 which is also a good approximation for the giant dunes observed in the North
 467 Sand Sea and South Sand Sea Station (Fig. 42 and Online Resource Fig. S5S4).
 468 Here, x and y are the streamwise and spanwise coordinates, $k = 2\pi/\lambda$ the
 469 wavenumber of the sinusoidal perturbation, α its crest orientation with respect
 470 to the x -direction (anticlockwise) and ξ_0 its amplitude. The two components
 471 of the basal shear stress $\tau = \rho_0 u_* \mathbf{u}_*$, constant in the flat bottom reference
 472 case, can then be generically written as:

$$\tau_x = \tau_0 \left(1 + k \xi_0 \sqrt{\mathcal{A}_x^2 + \mathcal{B}_x^2} \cos [k (\cos(\alpha)y - \sin(\alpha)x) + \phi_x] \right), \quad (4)$$

$$\tau_y = \tau_0 k \xi_0 \sqrt{\mathcal{A}_y^2 + \mathcal{B}_y^2} \cos [k (\cos(\alpha)y - \sin(\alpha)x) + \phi_y], \quad (5)$$

473 where τ_0 is the reference basal shear stress on a flat bed. We have defined
 474 the phase $\phi_{x,y} = \tan^{-1}(\mathcal{B}_{x,y}/\mathcal{A}_{x,y})$ from the in-phase and in-quadrature hydrodynamical coefficients $\mathcal{A}_{x,y}$ and $\mathcal{B}_{x,y}$. They are functions of k and of the
 475 flow conditions, i.e the bottom roughness, the vertical flow structure and the
 476 incident flow direction, and the theoretical framework developed in the above
 477 cited papers proposes methods to compute them in the linear regime.

478 Following Andreotti et al. (2012), the effect of the incident wind direction
 479 can be approximated by the following expressions:

$$\mathcal{A}_x = \mathcal{A}_0 \sin^2 \alpha, \quad (6)$$

$$\mathcal{B}_x = \mathcal{B}_0 \sin^2 \alpha, \quad (7)$$

$$\mathcal{A}_y = -\frac{1}{2} \mathcal{A}_0 \cos \alpha \sin \alpha, \quad (8)$$

$$\mathcal{B}_y = -\frac{1}{2} \mathcal{B}_0 \cos \alpha \sin \alpha, \quad (9)$$

481 where \mathcal{A}_0 and \mathcal{B}_0 are now two coefficients independent of the dune orientation
 482 α , corresponding to the transverse case ($\alpha = 90^\circ$). For-In the case of a fully
 483 turbulent boundary layer capped by a stratified atmosphere, these coefficients
 484 depend on kH , kz_0 , \mathcal{F} and \mathcal{F}_I (Andreotti et al. 2009). In this study For their
 485 computation, we assume here a constant hydrodynamic roughness $z_0 \simeq 1$ mm
 486 (Online Resource section 1). For the considered giant dunes, this leads to
 487 $kz_0 \simeq 2 \cdot 10^{-6}$, as their wavelength is $\lambda \simeq 2.4$ km (or $k \simeq 2 \cdot 10^{-3}$ m $^{-1}$). Values
 488 of z_0 extracted from field data indeed typically fall between 0.1 mm and 10
 489 mm (Sherman and Farrell 2008; Field and Pelletier 2018). Importantly, \mathcal{A}_0
 490 and \mathcal{B}_0 do not vary much in the corresponding range of kz_0 (Fourrière et al.
 491 2010), and the results presented here are robust with respect to this choice.

492 With capping layer height and Froude numbers computed from the ERA5-
 493 Land time series, the corresponding \mathcal{A}_0 and \mathcal{B}_0 can be deduced, as displayed
 494 in Online Resource Fig. ??S13. Interestingly, it shows similar regimes as in
 495 the diagrams of Fig. ??S13 and Online Resource Fig. ??S11a,b, supporting the
 496 underlying physics. However, the agreement is qualitative only. Further, the
 497 linearity assumption of the theoretical framework requires $(|\tau| - \tau_0)/\tau_0 \ll 1$,
 498 which translates into $k\xi\sqrt{\mathcal{A}_0^2 + \mathcal{B}_0^2} \ll 1$. In our case, the giant dune morphol-
 499 ogy gives $k\xi_0 \simeq 0.1$, which means that one quits the regime of validity of the
 500 linear theory when the coefficient modulus $\sqrt{\mathcal{A}_0^2 + \mathcal{B}_0^2}$ becomes larger than a
 501 few units. In accordance with the theoretical expectations, these coefficients
 502 present values on the order of unity ($\mathcal{A}_0 \simeq 3$ and $\mathcal{B}_0 \simeq 1$) in unconfined situations
 503 (Claudin et al. 2013; Lü et al. 2021). In contrast and as illustrated in
 504 Online Resource Fig. ??S13a,b, larger values are predicted in case of strong
 505 confinement, which does not allow us to proceed to further quantitative com-
 506 parison with the data.

507 Finally, the linear model is also able to reproduce the enhancement of
 508 the flow deflection over the sinusoidal ridges when $\sqrt{\mathcal{A}_0^2 + \mathcal{B}_0^2}$ is increased
 509 (Online Resource Fig. ??S13). Here, using $k\xi_0 \simeq 0.1$ to be representative of
 510 the amplitude of the giant dunes at the North Sand Sea station, the coefficient
 511 modulus is bounded to 10.

512 **Appendix 2: Sediment transport and dune morphodynamics**

513 We summarise in this appendix the sediment transport and dune morphodynamics
 514 theoretical framework leading to the prediction of sand fluxes and dune
 515 orientations from wind data.

516 *Sediment transport* — The prediction of sand fluxes from wind data has been
 517 a long standing issue in aeolian geomorphological studies (Fryberger and Dean
 518 1979; Pearce and Walker 2005; Sherman and Li 2012; Shen et al. 2019). Based
 519 on laboratory studies in wind tunnels (Rasmussen et al. 1996; Iversen and
 520 Rasmussen 1999; Creyssels et al. 2009; Ho et al. 2011), as well as physical
 521 considerations (Ungar and Haff 1987; Andreotti 2004; Durán et al. 2011; Pähzt
 522 and Durán 2020), it has been shown that the steady saturated saltation flux
 523 over a flat sand bed depends linearly on the shear stress:

$$\frac{q_{\text{sat}}}{Q} = \Omega \sqrt{\Theta_{\text{th}}} (\Theta - \Theta_{\text{th}}), \quad (10)$$

524 where Ω is a proportionality constant, $Q = d\sqrt{(\rho_s - \rho_0)gd/\rho_0}$ is a character-
 525 istic flux, $\Theta = \rho_0 u_*^2 / (\rho_s - \rho_0)gd$ the Shields number, and Θ_{th} its threshold
 526 value below which saltation vanishes. $\rho_s = 2.6 \text{ g cm}^{-3}$ and $d = 180 \mu\text{m}$ are
 527 the grain density and diameter, and g is the gravitational acceleration. The
 528 shear velocity, and consequently the Shields number as well as the sediment
 529 flux, are time dependent.

530 Recently, Pähzt and Durán (2020) suggested an additional quadratic term
 531 in Shields to account for grain-grain interactions within the transport layer at
 532 strong wind velocities:

$$\frac{q_{\text{sat}, t}}{Q} = \frac{2\sqrt{\Theta_{\text{th}}}}{\kappa\mu} (\Theta - \Theta_{\text{th}}) \left(1 + \frac{C_M}{\mu} [\Theta - \Theta_{\text{th}}] \right), \quad (11)$$

533 where $\kappa = 0.4$ is the von Kármán constant, $C_M \simeq 1.7$ a constant and $\mu \simeq 0.6$ is
 534 a friction coefficient, taken to be the avalanche slope of the granular material.
 535 The fit of this law to the experimental data of Creyssels et al. (2009) and
 536 Ho et al. (2011) gives $\Theta_{\text{th}} = 0.0035$. The fit of Eq. 10 on these same data
 537 similarly gives $\Omega \simeq 8$ and $\Theta_{\text{th}} = 0.005$. The sand flux angular distributions
 538 and the dune orientations in Fig. 6–9 are calculated using this law (11). We
 539 have checked that using the ordinary linear relationship (10) instead does not
 540 change the predicted dune orientations by more than a few degrees.

541 *Dune orientations* — Dune orientations are predicted with the dimensional
 542 model of Courrech du Pont et al. (2014), from the sand flux time series com-
 543 puted with the above transport law. Two orientations are possible depending
 544 on the mechanism dominating the dune growth: elongation or bed instability.
 545 The orientation α corresponding to the bed instability is then the one that
 546 maximises the following growth rate (Rubin and Hunter 1987):

$$\sigma \propto \frac{1}{H_d W_d T} \int_0^T q_{\text{crest}} |\sin(\theta - \alpha)| dt, \quad (12)$$

547 where θ is the wind orientation measured with respect to the same reference
 548 as α , and H_d and W_d are dimensional constants respectively representing the
 549 dune height and width. The integral runs over a time T , which must be repre-
 550 sentative of the characteristic period of the wind regime. The flux at the crest
 551 is expressed as:

$$q_{\text{crest}} = q_{\text{sat}} [1 + \gamma |\sin(\theta - \alpha)|], \quad (13)$$

552 where the flux-up ratio γ has been calibrated to 1.6 using field studies, under-
 553 water laboratory experiments and numerical simulations. Predictions of the
 554 linear analysis of Gadal et al. (2019) and Delorme et al. (2020) give similar
 555 results.

556 Similarly, the dune orientation corresponding to the elongation mechanism
 557 is the one that verifies:

$$\tan(\alpha) = \frac{\langle q_{\text{crest}}(\alpha) \mathbf{e}_\theta \rangle \cdot \mathbf{e}_{WE}}{\langle q_{\text{crest}}(\alpha) \mathbf{e}_\theta \rangle \cdot \mathbf{e}_{SN}}, \quad (14)$$

558 where $\langle \cdot \rangle$ denotes a vectorial time average. The unitary vectors \mathbf{e}_{WE} , \mathbf{e}_{SN} and
 559 \mathbf{e}_θ are in the West-East, South-North and wind directions, respectively.

560 The resulting computed dune orientations, blue and red arrows in Fig. 69,
 561 then depend on a certain number of parameters (grain properties, flux-up ratio,
 562 etc.), for which we take typical values for aeolian sandy deserts. Due to the lack
 563 of measurements in the studied places, some uncertainties can be expected. We
 564 therefore run a sensitivity test by calculating the dune orientations for grain
 565 diameters ranging from 100 μm to 400 μm and for a speed-up ratio between
 566 0.1 and 10 (wedges in Fig. 69).

567 References

- 568 Andreotti B (2004) A two-species model of aeolian sand transport. *J Fluid
569 Mech* 510:47–70
- 570 Andreotti B, Claudin P, Douady S (2002) Selection of dune shapes and veloc-
571 ities part 1: Dynamics of sand, wind and barchans. *The European Physical
572 Journal B-Condensed Matter and Complex Systems* 28:321–339
- 573 Andreotti B, Fourrière A, Ould-Kaddour F, Murray B, Claudin P (2009) Gi-
574 ant aeolian dune size determined by the average depth of the atmospheric
575 boundary layer. *Nature* 457:1120–1123
- 576 Andreotti B, Claudin P, Devauchelle O, Durán O, Fourrière A (2012) Bedforms
577 in a turbulent stream: ripples, chevrons and antidunes. *J Fluid Mech* 690:94–
578 128
- 579 Ashkenazy Y, Yizhaq H, Tsoar H (2012) Sand dune mobility under climate
580 change in the kalahari and australian deserts. *Climatic Change* 112:901–923
- 581 Baddock M, Livingstone I, Wiggs G (2007) The geomorphological significance
582 of airflow patterns in transverse dune interdunes. *Geomorphology* 87:322–
583 336
- 584 Bagnold RA (1941) *The Physics of Blown Sand and Desert Dunes*. London :
585 Methuen : Chapman & Hall
- 586 Baines PG (1995) Topographic effects in stratified flows. Cambridge university
587 press
- 588 Bauer BO, Sherman DJ, Wolcott JF (1992) Sources of uncertainty in shear
589 stress and roughness length estimates derived from velocity profiles. *The
590 Professional Geographer* 44:453–464
- 591 Belcher S, Hunt J (1998) Turbulent flow over hills and waves. *Annu Rev Fluid
592 Mech* 30:507–538
- 593 Blumberg DG, Greeley R (1996) A comparison of general circulation model
594 predictions to sand drift and dune orientations. *J Clim* 9:3248–3259
- 595 Bristow NR, Best J, Wiggs GFS, Nield JM, Baddock MC, Delorme P, Chris-
596 tensen KT (2022) Topographic perturbation of turbulent boundary layers
597 by low-angle, early-stage aeolian dunes. *Earth Surf Process Landf* n/a, DOI
598 <https://doi.org/10.1002/esp.5326>
- 599 Brookfield M (1977) The origin of bounding surfaces in ancient aeolian sand-
600 stones. *Sedimentology* 24:303–332
- 601 Brown S, Nickling WG, Gillies JA (2008) A wind tunnel examination of shear
602 stress partitioning for an assortment of surface roughness distributions. *J
603 Geophys Res* 113:F02S06
- 604 Chandler C, Radebaugh J, McBride J, Morris T, Narteau C, Arnold K, Lorenz
605 R, Barnes J, Hayes A, Rodriguez S, Rittenour T (2022) Near-surface struc-
606 ture of a large linear dune and an associated crossing dune of the northern
607 Namib Sand Sea from ground penetrating radar: Implications for the his-
608 tory of large linear dunes on Earth and Titan. *Aeolian Research* 57:100813,
609 DOI <https://doi.org/10.1016/j.aeolia.2022.100813>
- 610 Chang H, Simons D (1970) The bed configuration of straight sand-bed channels
611 when flow is nearly critical. *J Fluid Mech* 42:491–495

- 612 Charru F, Andreotti B, Claudin P (2013) Sand ripples and dunes. *Annu Rev
613 Fluid Mech* 45:469–493
- 614 Claudin P, Wiggs G, Andreotti B (2013) Field evidence for the upwind velocity
615 shift at the crest of low dunes. *Boundary-Layer Meteorol* 148:195–206
- 616 Claudin P, Durán O, Andreotti B (2017) Dissolution instability and roughen-
617 ing transition. *J Fluid Mech* 832:R2
- 618 Claudin P, Louge M, Andreotti B (2021) Basal pressure variations induced by
619 a turbulent flow over a wavy surface. *Frontiers in Physics* 9:682564
- 620 Colombini M (2004) Revisiting the linear theory of sand dune formation. *J
621 Fluid Mech* 502:1–16
- 622 Courrech du Pont S (2015) Dune morphodynamics. *C R Phys* 16:118–138
- 623 Courrech du Pont S, Narteau C, Gao X (2014) Two modes for dune orientation.
624 *Geology* 42:743–746
- 625 Creyssels M, Dupont P, El Moctar AO, Valance A, Cantat I, Jenkins JT, Pasini
626 JM, Rasmussen KR (2009) Saltating particles in a turbulent boundary layer:
627 experiment and theory. *J Fluid Mech* 625:47–74
- 628 de Winter W, Donker J, Sterk G, Van Beem J, Ruessink G (2020) Regional
629 versus local wind speed and direction at a narrow beach with a high and
630 steep foredune. *Plos one* 15:e0226983
- 631 Dee DP, Uppala SM, Simmons AJ, Berrisford P, Poli P, Kobayashi S, Andrae
632 U, Balmaseda M, Balsamo G, Bauer dP, et al. (2011) The ERA-Interim
633 reanalysis: Configuration and performance of the data assimilation system.
634 *Q J R Meteorol Soc* 137:553–597
- 635 Delorme P, Wiggs G, Baddock M, Claudin P, Nield J, Valdez A (2020) Dune
636 initiation in a bimodal wind regime. *J Geophys Res* 125:e2020JF005757
- 637 Durán O, Claudin P, Andreotti B (2011) On aeolian transport: Grain-scale
638 interactions, dynamical mechanisms and scaling laws. *Aeolian Res* 3:243–
639 270
- 640 Durran DR (1990) Mountain waves and downslope winds. In: *Atmospheric
641 processes over complex terrain*, Springer, pp 59–81
- 642 Dyer A (1974) A review of flux-profile relationships. *Boundary-Layer Meteorol*
643 7:363–372
- 644 Ewing RC, Kocurek G, Lake LW (2006) Pattern analysis of dune-field param-
645 eters. *Earth Surf Process Landf* 31:1176–1191
- 646 Farr TG, Rosen PA, Caro E, Crippen R, Duren R, Hensley S, Kobrick M,
647 Paller M, Rodriguez E, Roth L, et al. (2007) The shuttle radar topography
648 mission. *Rev Geophys* 45
- 649 Fernando H, Mann J, Palma J, Lundquist JK, Barthelmie RJ, Belo-Pereira M,
650 Brown W, Chow F, Gerz T, Hocut C, et al. (2019) The perdigão: Peering
651 into microscale details of mountain winds. *Bull Am Meteorol Soc* 100:799–
652 819
- 653 Field JP, Pelletier JD (2018) Controls on the aerodynamic roughness length
654 and the grain-size dependence of aeolian sediment transport. *Earth Surf
655 Process Landf* 43:2616–2626
- 656 Finnigan J, Raupach M, Bradley E, Aldis G (1990) A wind tunnel study
657 of turbulent flow over a two-dimensional ridge. *Boundary-Layer Meteorol*

- 658 50:277–317
- 659 Finnigan J, Ayotte K, Harman I, Katul G, Oldroyd H, Patton E, Poggi D,
660 Ross A, Taylor P (2020) Boundary-layer flow over complex topography.
Boundary-Layer Meteorol 177:247–313
- 662 Flack K, Schultz M (2010) Review of hydraulic roughness scales in the fully
663 rough regime. Journal of Fluids Engineering 132:041203
- 664 Fourrière A, Claudin P, Andreotti B (2010) Bedforms in a turbulent stream:
665 formation of ripples by primary linear instability and of dunes by nonlinear
666 pattern coarsening. J Fluid Mech 649:287–328
- 667 Frederick KA, Hanratty TJ (1988) Velocity measurements for a turbulent non-
668 separated flow over solid waves. Exp Fluids 6:477–486
- 669 Fryberger SG, Dean G (1979) Dune forms and wind regime. A study of global
670 sand seas 1052:137–169
- 671 Gadal C, Narteau C, Courrech Du Pont S, Rozier O, Claudin P (2019) Incip-
672 ient bedforms in a bidirectional wind regime. J Fluid Mech 862:490–516
- 673 Gadal C, Narteau C, Courrech du Pont S, Rozier O, Claudin P (2020) Peri-
674 odicity in fields of elongating dunes. Geology 48:343–347
- 675 Gadal C, Delorme P, Narteau C, Wiggs G, Baddock M, Nield JM, Claudin
676 P (2022) Data used in 'Local wind regime induced by giant linear dunes:
677 comparison of ERA5-Land re-analysis with surface measurements'. DOI
678 10.5281/zenodo.6343138
- 679 Gao X, Narteau C, Gadal C (2021) Migration of reversing dunes against the
680 sand flow path as a singular expression of the speed-up effect. Journal of
681 Geophysical Research: Earth Surface 126(5):e2020JF005913
- 682 Garratt JR (1994) The atmospheric boundary layer. Earth-Science Reviews
683 37:89–134
- 684 Garvey B, Castro IP, Wiggs G, Bullard J (2005) Measurements of flows over
685 isolated valleys. Boundary-Layer Meteorol 117:417–446
- 686 Gong W, Ibbetson A (1989) A wind tunnel study of turbulent flow over model
687 hills. Boundary-Layer Meteorol 49:113–148
- 688 Gong W, Taylor P, Dörnbrack A (1996) Turbulent boundary-layer flow over
689 fixed aerodynamically rough two-dimensional sinusoidal waves. J Fluid Mech
690 312:1–37
- 691 Guérin A, Derr J, Du Pont SC, Berhanu M (2020) Streamwise dissolution
692 patterns created by a flowing water film. Phys Rev Lett 125:194502
- 693 Gunn A, Wanker M, Lancaster N, Edmonds D, Ewing R, Jerolmack
694 D (2021) Circadian rhythm of dune-field activity. Geophys Res Lett
695 48:e2020GL090924
- 696 Gunn A, Casasanta G, Di Liberto L, Falcini F, Lancaster N, Jerolmack DJ
697 (2022) What sets aeolian dune height? Nature communications 13(1):1–8
- 698 Harris CR, Millman KJ, van der Walt SJ, Gommers R, Virtanen P, Cournapeau
699 D, Wieser E, Taylor J, Berg S, Smith NJ, et al. (2020) Array program-
700 ming with numpy. Nature 585:357–362
- 701 Havholm KG, Kocurek G (1988) A preliminary study of the dynamics of
702 a modern draa, Algodones, southeastern California, USA. Sedimentology
703 35:649–669

- 704 Hersbach H, Bell B, Berrisford P, Hirahara S, Horányi A, Muñoz-Sabater J,
705 Nicolas J, Peubey C, Radu R, Schepers D, et al. (2020) The ERA5 global
706 reanalysis. *Q J R Meteorol Soc* 146:1999–2049
- 707 Hesp P, Illenberger W, Rust I, McLachlan A, Hyde R (1989) Some aspects of
708 transgressive dunefield and transverse dune geomorphology and dynamics,
709 south coast, South Africa. *Zeitschrift fur Geomorphologie*, Supplementband
710 73:111–123
- 711 Hesp PA, Hastings K (1998) Width, height and slope relationships and aero-
712 dynamic maintenance of barchans. *Geomorphology* 22:193–204
- 713 Hesp PA, Smyth TAG, Nielsen P, Walker IJ, Bauer BO, Davidson-Arnott R
714 (2015) Flow deflection over a foredune. *Geomorphology* 230:64–74
- 715 Ho TD, Valance A, Dupont P, Ould El Moctar A (2011) Scaling laws in aeolian
716 sand transport. *Phys Rev Lett* 106:4–7
- 717 Hood DR, Ewing RC, Roback KP, Runyon K, Avouac JP, McEnroe M (2021)
718 Inferring airflow across martian dunes from ripple patterns and dynamics.
719 *Frontiers in Earth Science* 9:702828
- 720 Howard AD (1977) Effect of slope on the threshold of motion and its applica-
721 tion to orientation of wind ripples. *Geological Society of America Bulletin*
722 88:853–856
- 723 Hu Z, Gao X, Lei J, Zhou N (2021) Geomorphology of aeolian dunes in the
724 western Sahara Desert. *Geomorphology* 392:107916
- 725 Hunt J, Leibovich S, Richards K (1988) Turbulent shear flows over low hills.
726 *Q J R Meteorol Soc* 114:1435–1470
- 727 Hunt JCR, Vilenski GG, Johnson ER (2006) Stratified separated flow around
728 a mountain with an inversion layer below the mountain top. *J Fluid Mech*
729 556:105–119
- 730 Hunter JD (2007) Matplotlib: A 2d graphics environment. *Computing in sci-
731 ence & engineering* 9:90–95
- 732 Hunter RE, Richmond BM, Alpha TR (1983) Storm-controlled oblique dunes
733 of the Oregon coast. *Geol Soc America Bull* 94:1450–1465
- 734 Iversen JD, Rasmussen KR (1999) The effect of wind speed and bed slope on
735 sand transport. *Sedimentology* 46:723–731
- 736 Jackson PS, Hunt JCR (1975) Turbulent wind flow over a low hill. *Q J R
737 Meteorol Soc* 101:929–955
- 738 Jiang Q (2014) Applicability of reduced-gravity shallow-water theory to atmo-
739 spheric flow over topography. *J Atmos Sci* 71:1460–1479
- 740 Jolivet M, Braucher R, Dovchintseren D, Hocquet S, Schmitt J, ASTER Team
741 (2021) Erosion around a large-scale topographic high in a semi-arid sedimen-
742 tary basin: Interactions between fluvial erosion, aeolian erosion and aeolian
743 transport. *Geomorphology* 386:107747
- 744 Kennedy JF (1963) The mechanics of dunes and antidunes in erodible-bed
745 channels. *J Fluid Mech* 16:521–544
- 746 Kim HG, Patel VC, Lee CM (2000) Numerical simulation of wind flow over
747 hilly terrain. *J Wind Eng Ind Aerodyn* 87:45–60
- 748 Kroy K, Sauermann G, Herrmann HJ (2002) Minimal model for aeolian sand
749 dunes. *Phys Rev E* 66:031302

- 750 Lancaster J, Lancaster N, Seely M (1984) Climate of the central Namib desert.
751 Madoqua 1984:5–61
- 752 Lancaster N (1985) Winds and sand movements in the Namib sand sea. *Earth
753 Surf Process Landf* 10:607–619
- 754 Lancaster N, Nickling W, Neuman CM, Wyatt V (1996) Sediment flux and
755 airflow on the stoss slope of a barchan dune. *Geomorphology* 17:55–62
- 756 Lewis HW, Mobbs SD, Lehning M (2008) Observations of cross-ridge flows
757 across steep terrain. *Q J R Meteorol Soc* 134:801–816
- 758 Liu ZYC, Zimbelman JR (2015) Recent near-surface wind directions inferred
759 from mapping sand ripples on martian dunes. *Icarus* 261:169–181
- 760 Livingstone I, Warren A (2019) Aeolian geomorphology: a new introduction.
761 Wiley
- 762 Livingstone I, Bristow C, Bryant RG, Bullard J, White K, Wiggs GFS, Baas
763 ACW, Bateman MD, Thomas DSG (2010) The Namib Sand Sea digital
764 database of aeolian dunes and key forcing variables. *Aeolian Res* 2:93–104
- 765 Lorenz R, Claudin P, Andreotti B, Radebaugh J, Tokano T (2010) A 3 km at-
766 mospheric boundary layer on Titan indicated by dune spacing and Huygens
767 data. *Icarus* 205:719–721
- 768 Lü P, Narteau C, Dong Z, Rozier O, Du Pont SC (2017) Unravelling raked
769 linear dunes to explain the coexistence of bedforms in complex dunefields.
770 *Nature Communications* 8:1–9
- 771 Lü P, Narteau C, Dong Z, Claudin P, Rodriguez S, An Z, Fernandez-Cascales
772 L, Gadal C, Courrech du Pont S (2021) Direct validation of dune instability
773 theory. *Proceedings of the National Academy of Sciences* 118
- 774 Mason P, Sykes R (1979) Flow over an isolated hill of moderate slope. *Q J R
775 Meteorol Soc* 105:383–395
- 776 McKenna Neuman C, Lancaster N, Nickling WG (1997) Relations between
777 dune morphology, air flow, and sediment flux on reversing dunes, Silver Peak,
778 Nevada. *Sedimentology* 44:1103–1111, DOI 10.1046/j.1365-3091.1997.d01-
779 61.x
- 780 Mizumura K (1995) Free-surface profile of open-channel flow with wavy bound-
781 ary. *J Hydraul Eng* 121:533–539
- 782 Monin AS, Obukhov AM (1954) Basic laws of turbulent mixing in the surface
783 layer of the atmosphere. *Contrib Geophys Inst Acad Sci USSR* 151:e187
- 784 Mulligan KR (1988) Velocity profiles measured on the windward slope of a
785 transverse dune. *Earth Surf Process Landf* 13:573–582
- 786 Muñoz-Sabater J, Dutra E, Agustí-Panareda A, Albergel C, Arduini G, Bal-
787 samo G, Boussetta S, Choulga M, Harrigan S, Hersbach H, et al. (2021)
788 ERA5-Land: A state-of-the-art global reanalysis dataset for land applica-
789 tions. *Earth Syst Sci Data* 13:4349–4383
- 790 Nield JM, King J, Wiggs GFS, Leyland J, Bryant RG, Chiverrell RC, Darby
791 SE, Eckhardt FD, Thomas DSG, Vircavs LH, Washington R (2014) Esti-
792 mating aerodynamic roughness over complex surface terrain. *J Geophys Res*
793 118:12948–12961
- 794 Nield JM, Wiggs GG, Baddock MC, Hipondoka MH (2017) Coupling lee-
795 side rainfall to avalanche characteristics in aeolian dune dynamics. *Geology*

- 796 45:271–274
- 797 Pähzt T, Durán O (2020) Unification of aeolian and fluvial sediment transport
798 rate from granular physics. *Phys Rev Lett* 124:168001
- 799 Pearce KI, Walker IJ (2005) Frequency and magnitude biases in the 'Fryberger'
800 model, with implications for characterizing geomorphically effective winds.
801 *Geomorphology* 68:39–55
- 802 Pelletier JD, Field JP (2016) Predicting the roughness length of turbulent flows
803 over landscapes with multi-scale microtopography. *Earth Surface Dynamics*
804 4:391–405
- 805 Poggi D, Katul G, Albertson J, Ridolfi L (2007) An experimental investigation
806 of turbulent flows over a hilly surface. *Phys Fluids* 19:036601
- 807 Rasmussen KR (1989) Some aspects of flow over coastal dunes. *Proceedings of*
808 the Royal Society of Edinburgh, Section B: Biological Sciences 96:129–147
- 809 Rasmussen KR, Iversen JD, Rautaheimo P (1996) Saltation and wind flow
810 interaction in a variable slope wind tunnel. *Geomorphology* 17:19–28
- 811 Raupach M (1992) Drag and drag partition on rough surfaces. *Boundary-Layer*
812 *Meteorol* 60:375–395
- 813 Rozier O, Narteau C, Gadat C, Claudin P, Courrech du Pont S (2019)
814 Elongation and stability of a linear dune. *Geophysical Research Letters*
815 46(24):14521–14530
- 816 Rubin DM, Hunter RE (1987) Bedform alignment in directionally varying
817 flows. *Science* 237:276–278
- 818 Runyon K, Bridges N, Ayoub F, Newman C, Quade J (2017) An integrated
819 model for dune morphology and sand fluxes on Mars. *Earth and Planetary*
820 *Science Letters* 457:204–212
- 821 Sauermann G, Andrade Jr J, Maia L, Costa U, Araújo A, Herrmann H
822 (2003) Wind velocity and sand transport on a barchan dune. *Geomorphology*
823 54:245–255
- 824 Seidel DJ, Zhang Y, Beljaars A, Golaz JC, Jacobson AR, Medeiros B (2012)
825 Climatology of the planetary boundary layer over the continental United
826 States and Europe. *J Geophys Res* 117:D17106
- 827 Shao Y (2008) Physics and modelling of wind erosion, vol 37. Springer Science
828 & Business Media
- 829 Shen Y, Zhang C, Huang X, Wang X, Cen S (2019) The effect of wind speed
830 averaging time on sand transport estimates. *Catena* 175:286–293
- 831 Sheridan PF, Vosper SB (2006) A flow regime diagram for forecasting lee
832 waves, rotors and downslope winds. *Meteorol Appl* 13:179–195
- 833 Sherman CA (1978) A mass-consistent model for wind fields over complex
834 terrain. *J Appl Meteorol Clim* 17:312–319
- 835 Sherman D, Farrell E (2008) Aerodynamic roughness lengths over movable
836 beds: Comparison of wind tunnel and field data. *J Geophys Res* 113:1–10
- 837 Sherman DJ, Li B (2012) Predicting aeolian sand transport rates: A reevalu-
838 ation of models. *Aeolian Res* 3:371–378
- 839 Smith AB, Jackson DWT, Cooper JAG (2017) Three-dimensional airflow and
840 sediment transport patterns over barchan dunes. *Geomorphology* 278:28–42

- 841 Song Q, Gao X, Lei J, Li S (2019) Spatial distribution of sand dunes and their
842 relationship with fluvial systems on the southern margin of the Taklimakan
843 Desert, China. *Geomatics, Natural Hazards and Risk* 10:2408–2428
- 844 Spalding DB (1961) A single formula for the law of the wall. *Journal of Applied
845 Mechanics* 28:455–458
- 846 Stull R (2006) 9 - the atmospheric boundary layer. In: Wallace JM, Hobbs PV
847 (eds) *Atmospheric Science* (Second Edition), second edition edn, Academic
848 Press, San Diego, pp 375–417
- 849 Stull RB (1988) An introduction to boundary layer meteorology, vol 13.
850 Springer Science & Business Media
- 851 Sullivan PP, McWilliams JC (2010) Dynamics of winds and currents coupled
852 to surface waves. *Annu Rev Fluid Mech* 42:19–42
- 853 Sweet M, Kocurek G (1990) An empirical model of aeolian dune lee-face air-
854 flow. *Sedimentology* 37:1023–1038
- 855 Sykes RI (1980) An asymptotic theory of incompressible turbulent boundary-
856 layer flow over a small hump. *J Fluid Mech* 101:647–670
- 857 Taylor P, Teunissen H (1987) The Askervein hill project: overview and back-
858 ground data. *Boundary-Layer Meteorol* 39:15–39
- 859 Taylor P, Mason P, Bradley E (1987) Boundary-layer flow over low hills.
860 *Boundary-Layer Meteorol* 39:107–132
- 861 Tsoar H, Yaalon DH (1983) Deflection of sand movement on a sinuous longi-
862 tudinal (seif) dune: use of fluorescent dye as tracer. *Sedimentary Geology*
863 36:25–39
- 864 Ungar JE, Haff PK (1987) Steady state saltation in air. *Sedimentology* 34:289–
865 299
- 866 Unsworth C, Parsons D, Hardy R, Reesink A, Best J, Ashworth P, Keevil G
867 (2018) The impact of nonequilibrium flow on the structure of turbulence
868 over river dunes. *Water Resour Res* 54:6566–6584
- 869 Uppala SM, Källberg P, Simmons AJ, Andrae U, Bechtold VDC, Fiorino M,
870 Gibson J, Haseler J, Hernandez A, Kelly G, et al. (2005) The ERA-40 re-
871 analysis. *Q J R Meteorol Soc* 131:2961–3012
- 872 Valance A, Rasmussen K, Ould El Moctar A, Dupont P (2015) The physics
873 of aeolian sand transport. *C R Phys* 16:1–13
- 874 Venditti JG, Best JL, Church M, Hardy RJ (2013) Coherent Flow Structures
875 at Earth's Surface. John Wiley & Sons
- 876 Virtanen P, Gommers R, Oliphant TE, Haberland M, Reddy T, Cournapeau
877 D, Burovski E, Peterson P, Weckesser W, Bright J, et al. (2020) Scipy 1.0:
878 fundamental algorithms for scientific computing in python. *Nature methods*
879 17:261–272
- 880 Vogelezang D, Holtslag A (1996) Evaluation and model impacts of alternative
881 boundary-layer height formulations. *Boundary-Layer Meteorol* 81:245–269
- 882 Vosper SB (2004) Inversion effects on mountain lee waves. *Q J R Meteorol Soc*
883 130:1723–1748
- 884 Walker I, Davidson-Arnott R, Bauer B, Hesp P, Delgado-Fernandez I, Oller-
885 head J, Smyth T (2017) Scale-dependent perspectives on the geomorphology
886 and evolution of beach-dune systems. *Earth-Science Review* 171:220–253

- 887 Walker IJ, Nickling WG (2002) Dynamics of secondary airflow and sediment
888 transport over and in the lee of transverse dunes. *Prog Phys Geogr* 26:47–75
- 889 Walker IJ, Hesp PA, Davidson-Arnott RG, Ollerhead J (2006) Topographic
890 steering of alongshore airflow over a vegetated foredune: Greenwich Dunes,
891 Prince Edward Island, Canada. *Journal of Coastal Research* 22:1278–1291
- 892 Walker IJ, Hesp PA, Davidson-Arnott RG, Bauer BO, Namikas SL, Ollerhead
893 J (2009) Responses of three-dimensional flow to variations in the angle of
894 incident wind and profile form of dunes: Greenwich Dunes, Prince Edward
895 Island, Canada. *Geomorphology* 105:127–138
- 896 Walmsley JL, Salmon J, Taylor P (1982) On the application of a model of
897 boundary-layer flow over low hills to real terrain. *Boundary-Layer Meteorol*
898 23:17–46
- 899 Weaver C, Wiggs G (2011) Field measurements of mean and turbulent airflow
900 over a barchan sand dune. *Geomorphology* 128:32–41
- 901 Werner BT, Kocurek G (1999) Bedform spacing from defect dynamics. *Geol-*
902 *ogy* 27:727–730
- 903 Wiggs G, Bullard J, Garvey B, Castro I (2002) Interactions between airflow
904 and valley topography with implications for aeolian sediment transport.
905 *Physical Geography* 23:366–380
- 906 Wood N (2000) Wind flow over complex terrain: a historical perspective and
907 the prospect for large-eddy modelling. *Boundary-Layer Meteorol* 96:11–32
- 908 Zhang C, Li Q, Zhou N, Zhang J, Kang L, Shen Y, Jia W (2016) Field obser-
909 vations of wind profiles and sand fluxes above the windward slope of a sand
910 dune before and after the establishment of semi-buried straw checkerboard
911 barriers. *Aeolian Res* 20:59–70
- 912 Zhang D, Yang X, Rozier O, Narteau C (2014) Mean sediment residence time in
913 barchan dunes. *Journal of Geophysical Research: Earth Surface* 119(3):451–
914 463
- 915 Zilker DP, Hanratty TJ (1979) Influence of the amplitude of a solid wavy wall
916 on a turbulent flow. part 2. separated flows. *J Fluid Mech* 90:257–271
- 917 Zilker DP, Cook GW, Hanratty TJ (1977) Influence of the amplitude of a solid
918 wavy wall on a turbulent flow. part 1. non-separated flows. *J Fluid Mech*
919 82:29–51

920 **Local wind regime induced by giant linear dunes**
 921 — Supplementary Material —

922 **C. Gadal* · P. Delorme · C. Narteau · G.F.S. Wiggs · M. Baddock ·**
 923 **J.M. Nield · P. Claudin**

924
 925 * Institut de Mécanique des Fluides de Toulouse, Université de Toulouse Paul
 926 Sabatier, CNRS, Toulouse INP-ENSEEIHT, Toulouse, France.
 927 cyril.gadal@imft.fr

928 **1. Shear velocity and calibration of the hydrodynamical roughness**

929 As the regionally predicted and locally measured velocities are available at
 930 different heights, we can not compare them directly. We therefore convert all
 931 velocities into shear velocities u_* , characteristic ~~of the turbulent~~ ~~the turbulent~~
 932 logarithmic velocity profile (Spalding 1961; Stull 1988):

$$\frac{u(z)}{u_*} = \frac{1}{\kappa} \ln \left(\frac{z}{z_0} \right), \quad (15)$$

933 where z is the vertical coordinate, $\kappa = 0.4$ the von Kármán constant and z_0 the
 934 hydrodynamic roughness. Note that, strickly speaking, this logarithmic profile
 935 is valid for a neutrally stratified ABL only. Vertical density gradients occuring
 936 in other conditions may thus induce large discrepancies (Monin and Obukhov 1954; Garratt 1994; Dyer 1974)
 937 . However, as our wind measurements are in the flow region close enough to
 938 the surface, where these effects are negligible, this logarithmic wind profile
 939 remains a fairly good approximation in all conditions (Gunn et al. 2021). Several
 940 measurements of hydrodynamic roughnesses are available (Raupach 1992;
 941 Bauer et al. 1992; Brown et al. 2008; Nield et al. 2014). In the absence of
 942 sediment transport, it is governed by the geometric features of the bed (Flack
 943 and Schultz 2010; Pelletier and Field 2016). When aeolian saltation occurs, it
 944 is rather controlled by the altitude of Bagnold's focal point (Durán et al. 2011;
 945 Valance et al. 2015), which depends on the wind velocity and grain properties
 946 (Sherman and Farrell 2008; Zhang et al. 2016; Field and Pelletier 2018).
 947 Whether associated with geometric features or with sediment transport, its
 948 typical order of magnitude is the millimetre scale on sandy surfaces.

949 We do not have precise velocity vertical profiles to be able to deduce an
 950 accurate value of z_0 in the various environments of the meteorological stations
 951 (vegetated, arid, sandy). Our approach is to rather select the hydrodynamic
 952 roughness which allows for the best possible matching between the regionally
 953 predicted and locally measured winds, i.e. minimising the relative difference δ
 954 between the wind vectors of both datasets:

$$\delta = \frac{\sqrt{\langle \| \mathbf{u}_{*,\text{era}} - \mathbf{u}_{*,\text{station}} \|^2 \rangle}}{\sqrt{\langle \| \mathbf{u}_{*,\text{era}} \|^2 \rangle \langle \| \mathbf{u}_{*,\text{station}} \|^2 \rangle}}, \quad (16)$$

where $\langle \cdot \rangle$ denotes time average. This parameter is computed for values of z_0 in ERA5-Land analysis ranging from 10^{-5} m to 10^{-2} m for the four different stations. Note that for the North Sand Sea and South Sand Sea stations, where the giant dunes feedback presumably affect the wind, we take into account the non-deflected winds only in the calculation of δ (with a 15° tolerance).

As shown in Online Resource Fig. S4S3, the minimum values of δ in the space $(z_0^{\text{ERA5Land}}, z_0^{\text{local}})$ form a line. We thus set the roughness in the ERA5-Land analysis to the typical value $z_0 = 10^{-3}$ m, and deduce the corresponding ones for the local stations. It leads to 2.7, 0.8, 0.1 and 0.5 mm for the Etosha West, North Sand Sea, Huab and South Sand Sea stations, respectively. Importantly, this approach somewhat impacts the calculation of the shear velocities, but not that of the wind directions. As such, most of our conclusions are independent of such a choice. However, it may affect the magnitude of the wind velocity attenuation/amplification in flow confinement situations.

2. Computation of the ABL characteristics

The estimation of the non-dimensional numbers associated with the ABL requires the computation of representative meteorological quantities. In arid areas, the vertical structure of the atmosphere can be approximated by a well mixed convective boundary layer of height H , topped by the stratified free atmosphere (Stull 1988; Shao 2008). In this context, one usually introduces the virtual potential temperature T_{vp} , which is a constant T_0 inside the boundary layer, and increases linearly in the FA (Online Resource Fig. S12S8a):

$$T_{\text{vp}}(z) = \begin{cases} T_0 & \text{for } z \leq H, \\ T_0 \left(1 + \frac{\Delta T_{\text{vp}}}{T_0} + \frac{N^2}{g}(z - H) \right) & \text{for } z \geq H, \end{cases} \quad (17)$$

where ΔT_{vp} is the temperature discontinuity at the capping layer and $N = \sqrt{g\partial_z T_{\text{vp}}/T_0}$ is the Brunt-Väisälä frequency, characteristic of the stratification. Note that, under the usual Boussinesq approximation, temperature and air density variations are simply related by $\delta T_{\text{vp}}/T_0 \simeq -\delta\rho/\rho_0$ (see Online Resource of Andreotti et al. (2009)), so that N can equivalently be defined from the density gradient as next to Eq. 4(1).

The ERA5 dataset provides vertical profiles of the geopotential ϕ , the actual temperature T and the specific humidity η at given pressure levels P . The vertical coordinate is then calculated as:

$$z = \frac{\phi R_t}{g R_t - \phi}, \quad (18)$$

where $R_t = 6371229$ m is the reference Earth radius and $g = 9.81$ m s $^{-2}$ is the gravitational acceleration. One also computes the virtual potential temperature as:

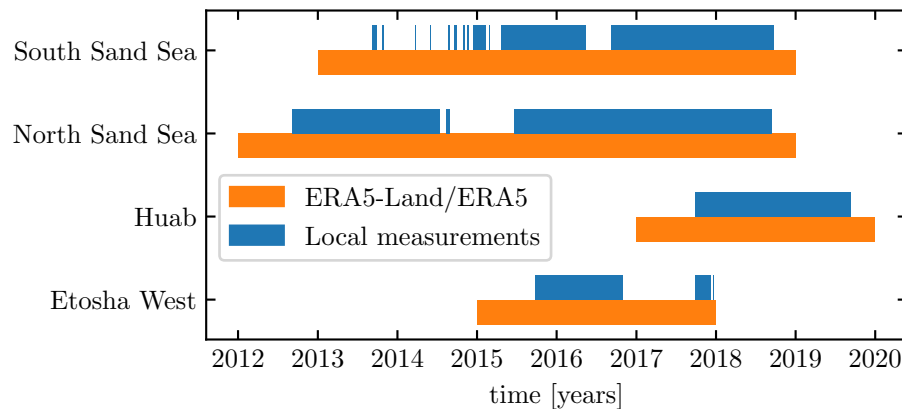
$$T_{\text{vp}} = T \left[1 + \left(\frac{M_d}{M_w} - 1 \right) \eta \right] \left(\frac{P_0}{P} \right)^{R/C_p}, \quad (19)$$

where $P_0 = 10^5$ Pa is the standard pressure, $R = 8.31$ J/K is the ideal gas constant, $C_p \simeq 29.1$ J/K is the air molar heat capacity, and $M_w = 0.018$ kg/Mol and $M_d = 0.029$ kg/Mol are the molecular masses of water and dry air respectively. The specific humidity is related to the vapour pressure p_w as

$$\eta = \frac{\frac{M_w}{M_d} p_w}{p - \left(1 - \frac{M_w}{M_d}\right) p_w}. \quad (20)$$

The ERA5 dataset also provides an estimate of the ABL depth H , based on the behaviour of the Richardson vertical profile. This dimensionless number is defined as the ratio of buoyancy and flow shear terms, and can be expressed as $\text{Ri} = N^2 / (\partial_z u)^2$. It vanishes in the lower well-mixed layer where T_{vp} is constant, and increases in the stratified FA. Following the method and calibration of Vogelegang and Holtlag (1996); Seidel et al. (2012), the value $\text{Ri}(z) \simeq 0.25$ has been shown to be a good empirical criterion to give $z \simeq H$ within a precision varying from 50% for the shallower ABL (e.g. at night) to 20% for situations of stronger convection.

Examples of vertical ~~profiles of the~~ virtual potential temperature ~~profiles~~ deduced from ERA5 are shown in Online Resource Fig. S12S8a. For each of them, an average temperature is computed below the ABL depth ($z < H$), and a linear function is fitted above, allowing us to extract the temperature jump ΔT_{vp} . Importantly, some profiles display a vertical structure that cannot be approximated by the simple form (17) used here (Online Resource Fig. S12S8b). In practice, we removed from the analysis all of those leading to the unphysical case $\Delta T_{vp} < 0$. We have noticed that these ‘ill-processed’ profiles dominantly occur in winter and are evenly spread across the hours of the day. Importantly, they represent $\simeq 12\%$ of the data only (Online Resource Fig. S12S8c,d), and we are thus confident that this data treatment does not affect our conclusions.



Gantt chart representing the valid time steps for the two data sets, for all stations.

Fig. S1 Photographs of the meteorological stations. **a:** South Sand Sea station. **b–e:** North Sand Sea station. **d:** Huab station. **e:** Etosha West station.

Gantt chart representing the valid time steps for the two data sets, for all stations.

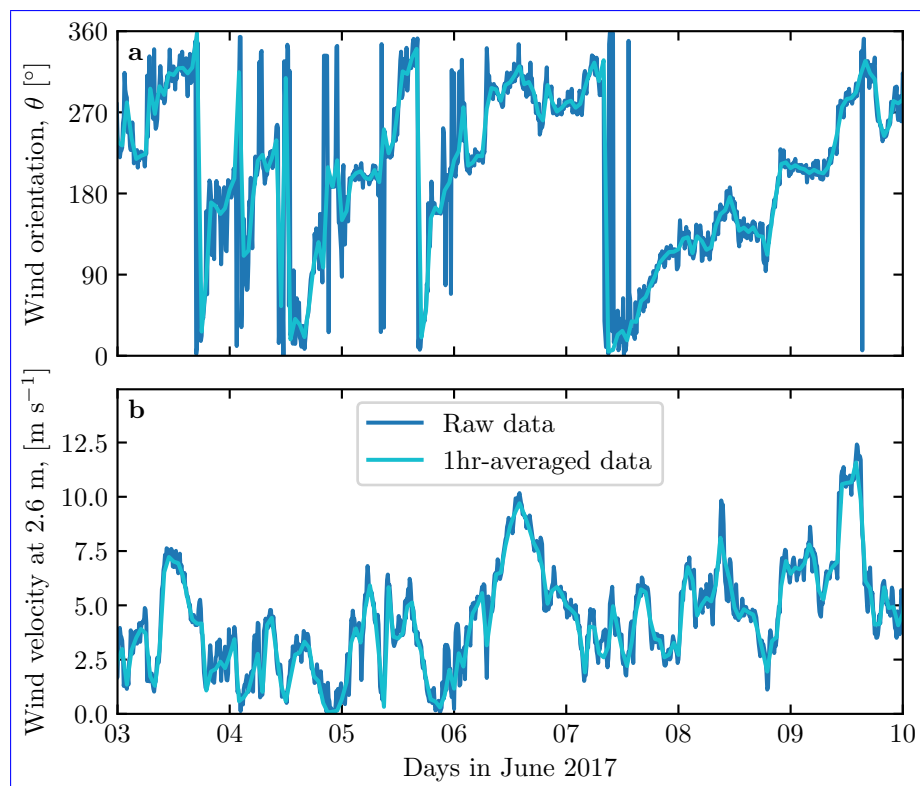


Fig. S2 Comparison between raw local wind measurements and hourly-averaged data for South Sand Sea station. **a:** wind direction. **b:** wind velocity at height 2.6 m.

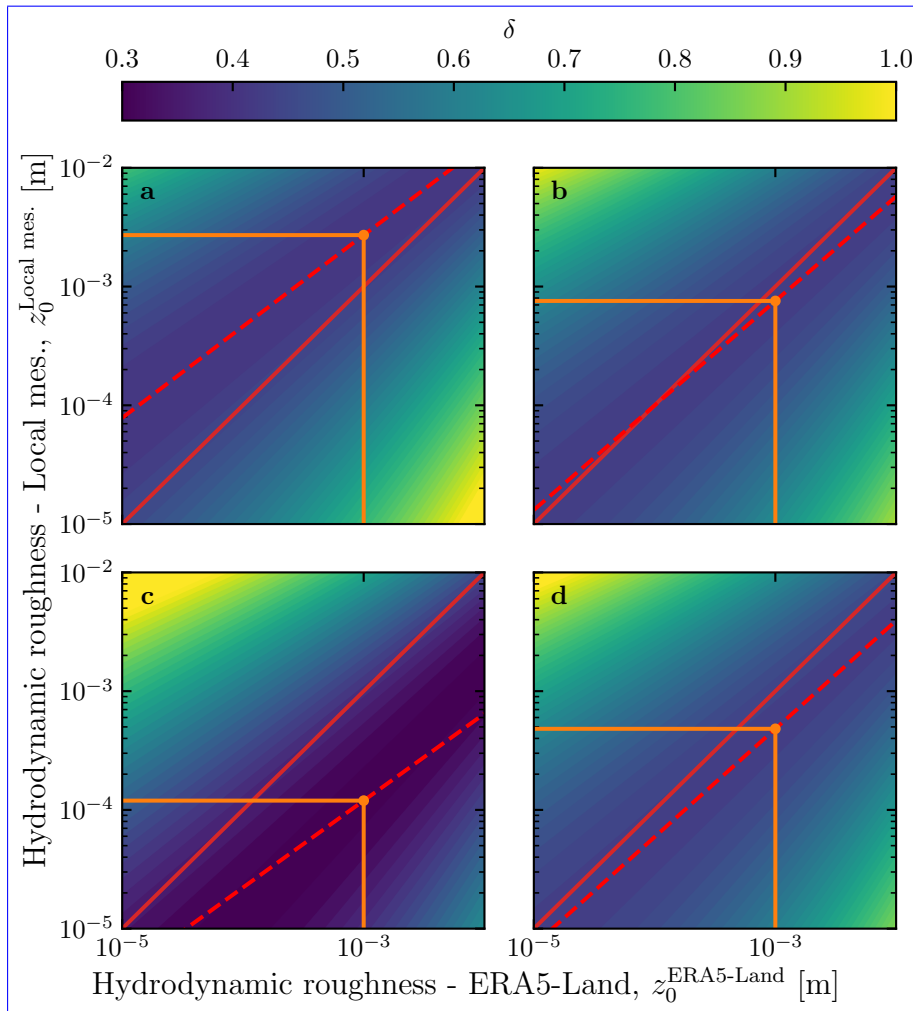


Fig. S3 Calibration of hydrodynamic roughness. The parameter δ (Eq. 16) quantifying the difference between local and predicted winds is shown as a function of the hydrodynamic roughnesses chosen for the ERA5-Land and for local winds, for the (a) Etosha West, (b) North Sand Sea, (c) Huab and (d) South Sand Sea stations. The red dashed and plain lines show the minima of δ and the identity line, respectively. The orange lines and dots highlight the chosen hydrodynamic roughnesses for the local winds deduced from setting $z_0^{\text{ERA5Land}} = 1$ $z_0^{\text{ERA5-Land}} = 1$ mm.

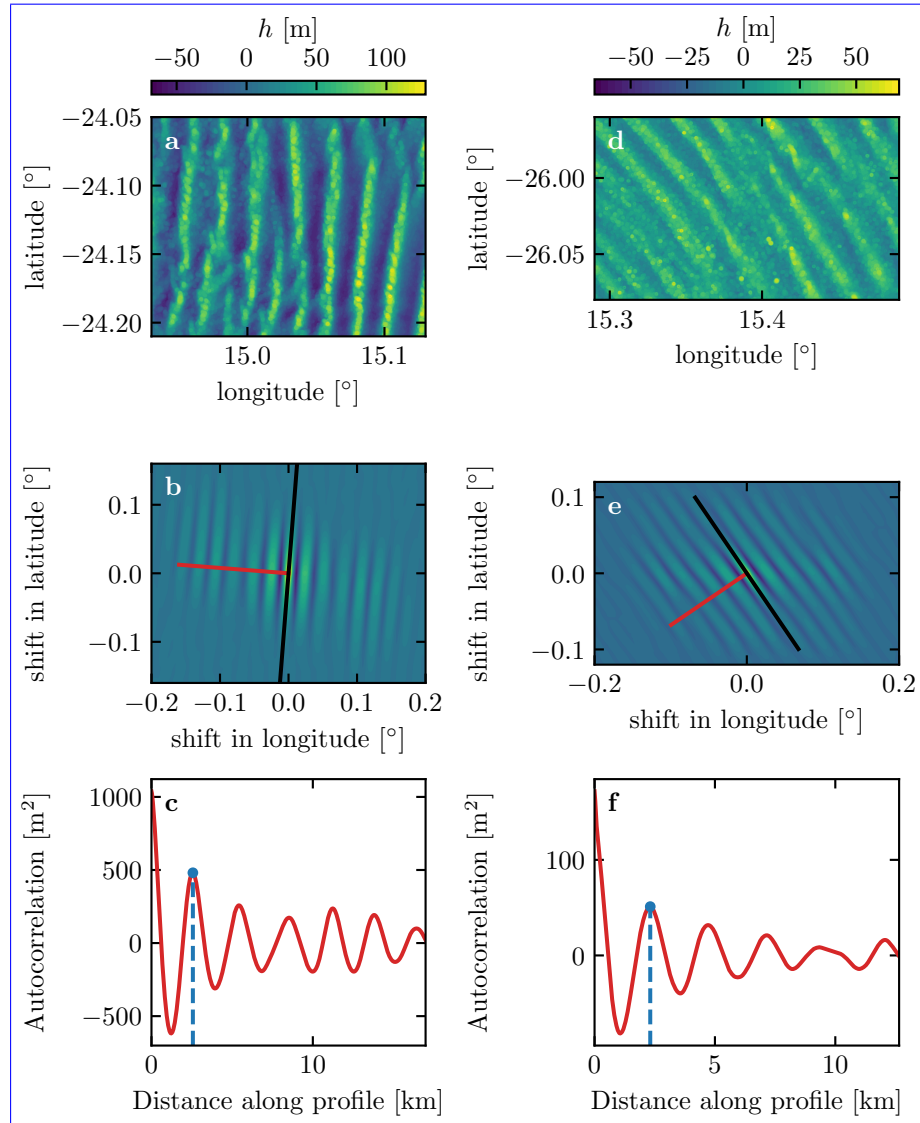


Fig. S4 Analysis of the DEMs of the North Sand Sea (left column – panels **a**, **b**, **c**) and South Sand Sea (right column – panels **d**, **e**, **f**) stations. **a–d**: Bed elevation detrended by a fitted second order polynomial base-line. **b–e**: Autocorrelation matrix shown in **color scale**. The black line shows the detected dune orientation, and the red line represents the autocorrelation profile along which the dune wavelength is calculated, displayed in **c–f**. The blue lines and dots show the first peak of the autocorrelation profile, whose abscissa gives the characteristic wavelength of the dune pattern.

Temporal comparison between the wind data coming from the ERA5-Land climate reanalysis (orange lines) and from the local measurements (blue lines). Coloured swathes indicate day (between 1000 UTC and 2200 UTC) and night (before 1000 UTC or after 2200 UTC). **a–b**: Huab station in summer. **b–c**: Huab station in winter. **d–e**: South Sand Sea station in summer. **f–g**: South Sand Sea station in winter.

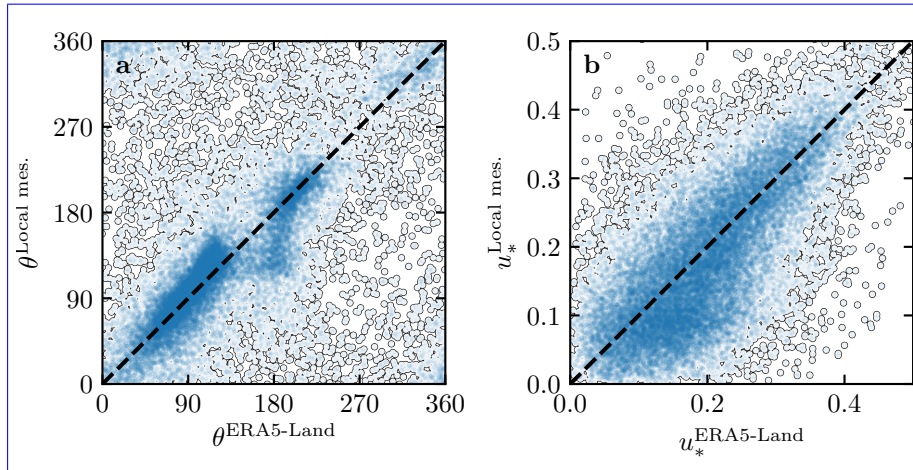


Fig. S5 Statistical comparison of the wind orientation (a) and velocity (b) between the ERA5-Land dataset and the local measurements for the Huab and Etosha West stations. Data point clustering around identity lines (dashed and black) provide evidence for agreement of the two sets.

Distributions of wind direction at the South Sand Sea Station for the ERA5-Land climate reanalysis (orange) and the local measurements (blue)—equivalent of Fig. 3. In each subplot, both distributions are plotted from the same time steps, selected with constraints on the wind direction (columns) and/or wind velocity (rows) in the ERA5-Land dataset. The gray vertical dashed lines indicate the dune orientation. The numbers at the top centre give the percentage of time steps selected in each sub-range, as well as the percentage of them corresponding to the day (between 1000 UTC and 2200 UTC). The purple frame highlights the regime (small wind velocities, nocturnal summer wind) during which the wind data from both datasets differ.

Distributions of wind direction at the Huab and Etosha West stations for the ERA5-Land climate reanalysis (orange) and the local measurements (blue). In each subplot, both distributions are plotted from the same time steps, selected with constraints on the wind velocity (rows) in the ERA5-Land dataset. The numbers at the top centre give the percentage of time steps selected in each sub-range, as well as the percentage of them corresponding to the day (between 1000 UTC and 2200 UTC). Compared to the North and South Namib stations (Fig. 3 and Fig. S8), histograms match for high and low velocities.

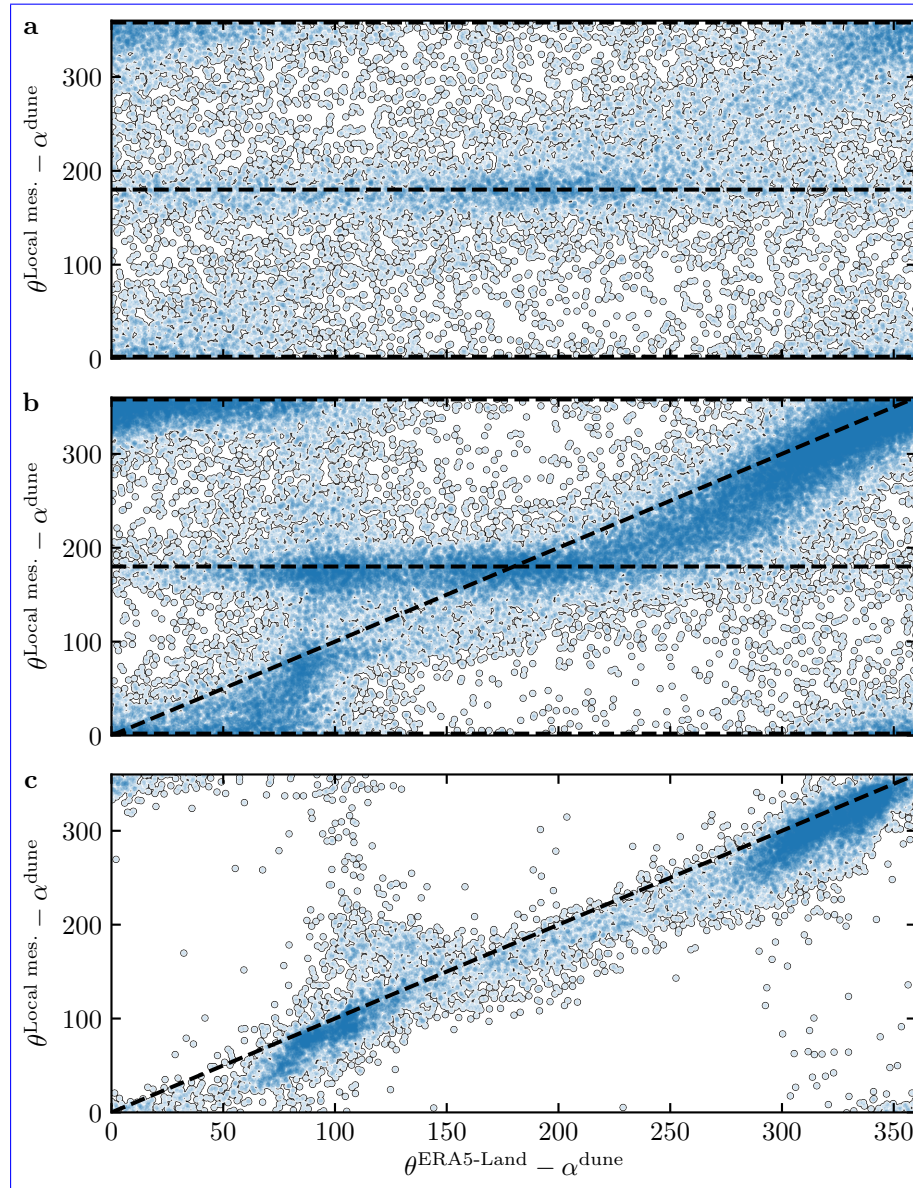


Fig. S6 Statistical comparison of the wind orientation between the ERA5-Land dataset and the local measurements for the South Sand Sea and North Sand Sea stations, for different velocity ranges. a: $u_{*,\text{ERA}} < 0.1 \text{ m s}^{-1}$ $u^{\text{ERA5-Land}} < 0.1 \text{ m s}^{-1}$. b: $0.1 < u_{*,\text{ERA}} \leq 0.25 \text{ m s}^{-1}$ $0.1 < u^{\text{ERA5-Land}} \leq 0.25 \text{ m s}^{-1}$. c: $u_{*,\text{ERA}} \geq 0.25 \text{ m s}^{-1}$ $u^{\text{ERA5-Land}} \geq 0.25 \text{ m s}^{-1}$. The measured dune orientations are subtracted to the wind orientation, which allows us to plot both stations on the same graph. Black dashed lines indicate locally measured orientations aligned with the dune crests (here 0°, 180° and 360° – panels a, b), as well as the identity lines (panels b, c).

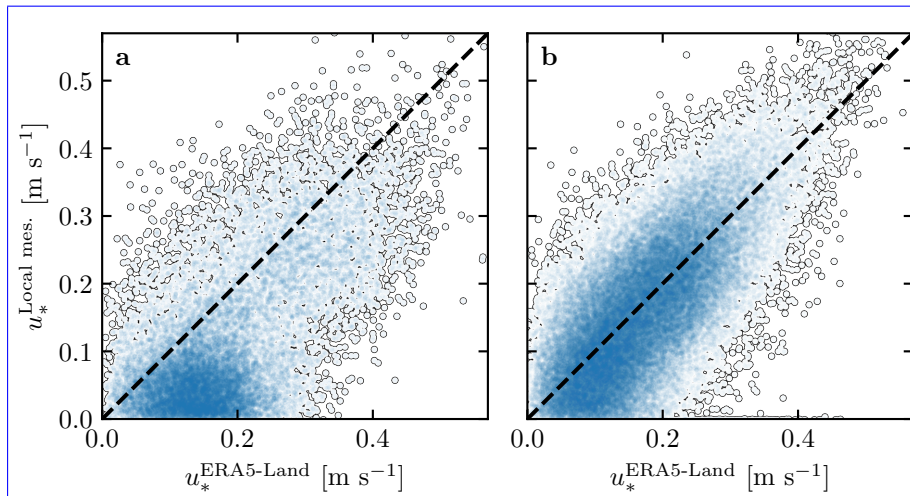


Fig. S7 Statistical comparison of the wind velocity between the ERA5-Land dataset and the local measurements for the South Sand Sea and North Sand Sea stations. **a:** Nocturnal summer easterly wind. **b:** Diurnal southerly wind. Black dashed lines are identity lines. The angle ranges used to select diurnal and nocturnal summer winds are the same as those in [FigFigs. 3–4](#) and [Online Resourcee FigFigs. S86 of the main article](#).

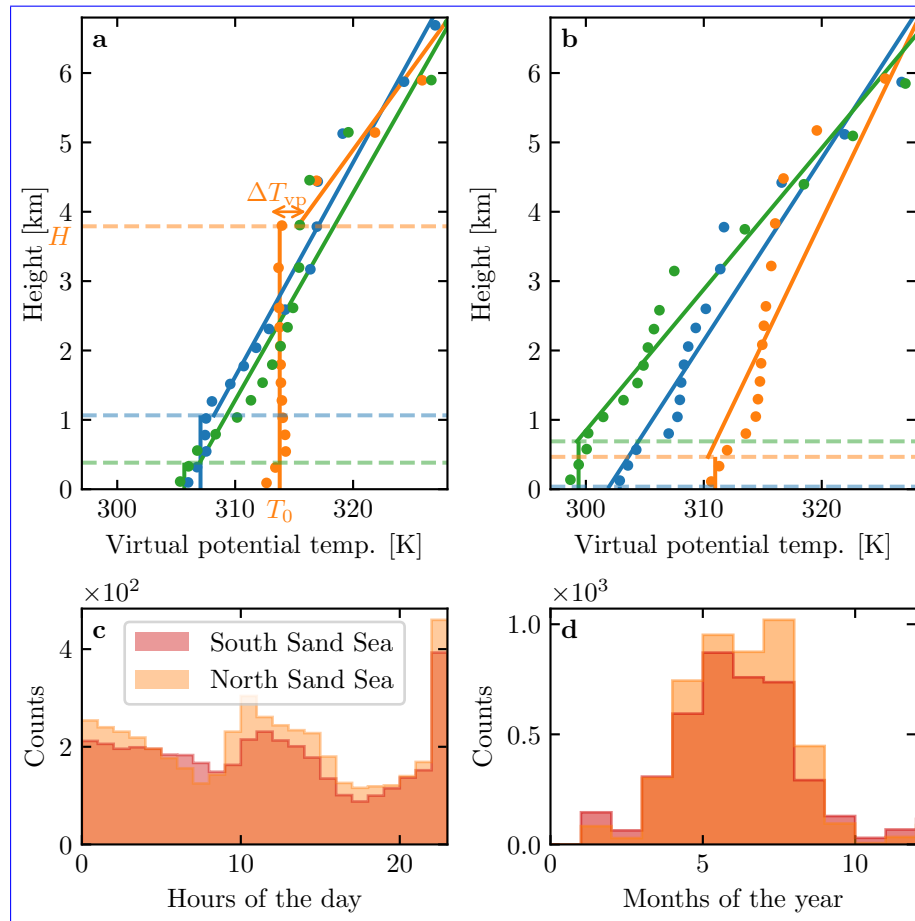


Fig. S8 a: Vertical profiles of the virtual potential temperature at three different times (blue: 29/11/2012 - 11:00–11:00 UTC, orange: 21/03/2017 - 12:00–12:00 UTC, green: 21/03/2017 - 20:00–20:00 UTC) at the South Sand Sea station. Dots: data from the ERA5 reanalysis. Dashed lines: boundary layer height given by the ERA5 reanalysis. Plain lines: vertical (ABL) and linear (FA) fits to estimate the quantities displayed in Online Resource Fig. S13S9. b: Examples of ill-processed vertical profiles at three different times (blue: 2/12/2013 - 23:00–23:00 UTC, orange: 20/03/2017 - 00:00–00:00 UTC, green: 14/07/2017 - 14:00–14:00 UTC) at the South Sand Sea station. c: Hourly distribution Distribution of ill-processed vertical profiles dat South (orange) and North (light orange) Sand Sea station: Monthly distribution of ill-processed vertical profileshourly (c) and monthly (d) counts.

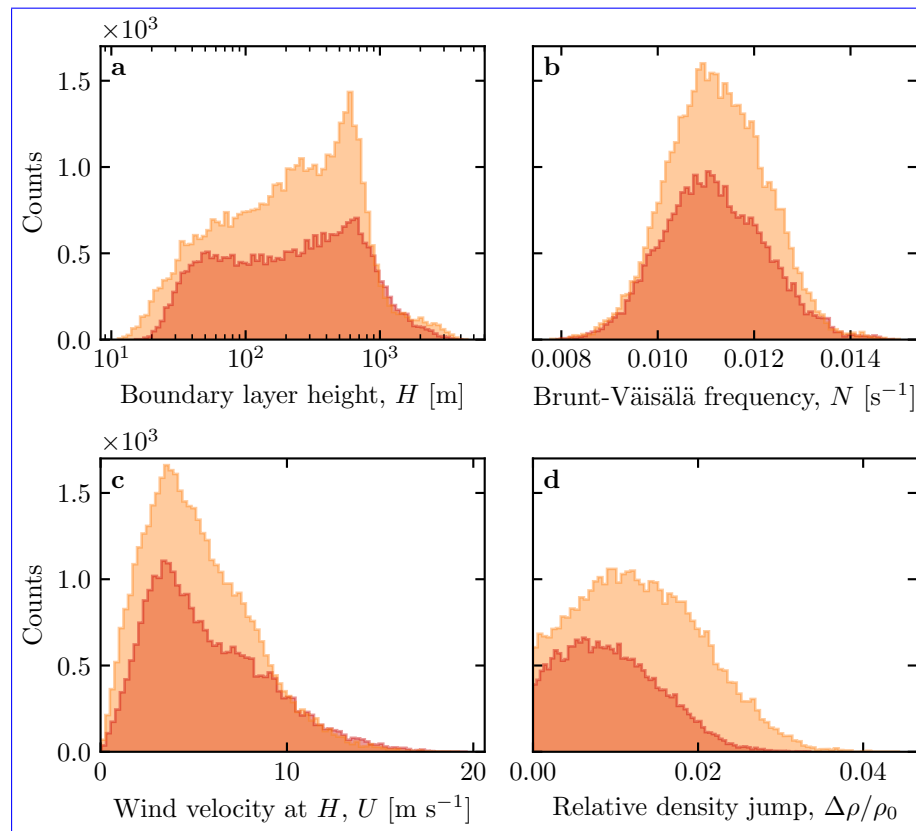


Fig. S9 Distributions of the meteorological parameters resulting from the processing of the ERA5-Land data for the South Sand Sea (**blueorange**) and the North Sand Sea (**light orange**) stations.

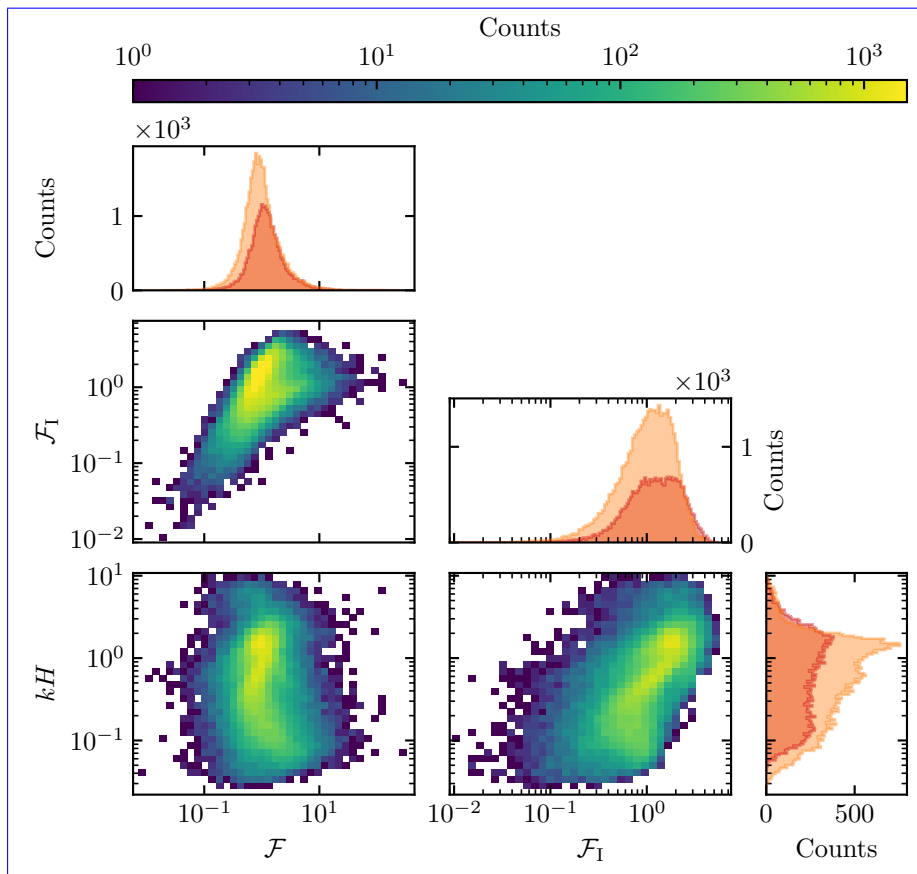


Fig. S10 Non-dimensional parameters distributions. For the marginal distributions, the light orange corresponds to the South Sand Sea station, and the blue to the North Sand Sea station.

Regime diagrams of the wind deviation δ_θ and relative attenuation/amplification δ_u in the spaces (\mathcal{F}_I, kH) and $(\mathcal{F}_I, \mathcal{F})$, containing the data from both the North Sand Sea and South Sand Sea stations. Green dashed lines empirically delimit the different regimes. The point density in each bin of the diagrams is shown in Online Resource Fig. S14 – 95% of the data occur in the range $-1 < \delta u < 1$. The similar regime diagrams in the space (\mathcal{F}, kH) are shown in Fig. 5.

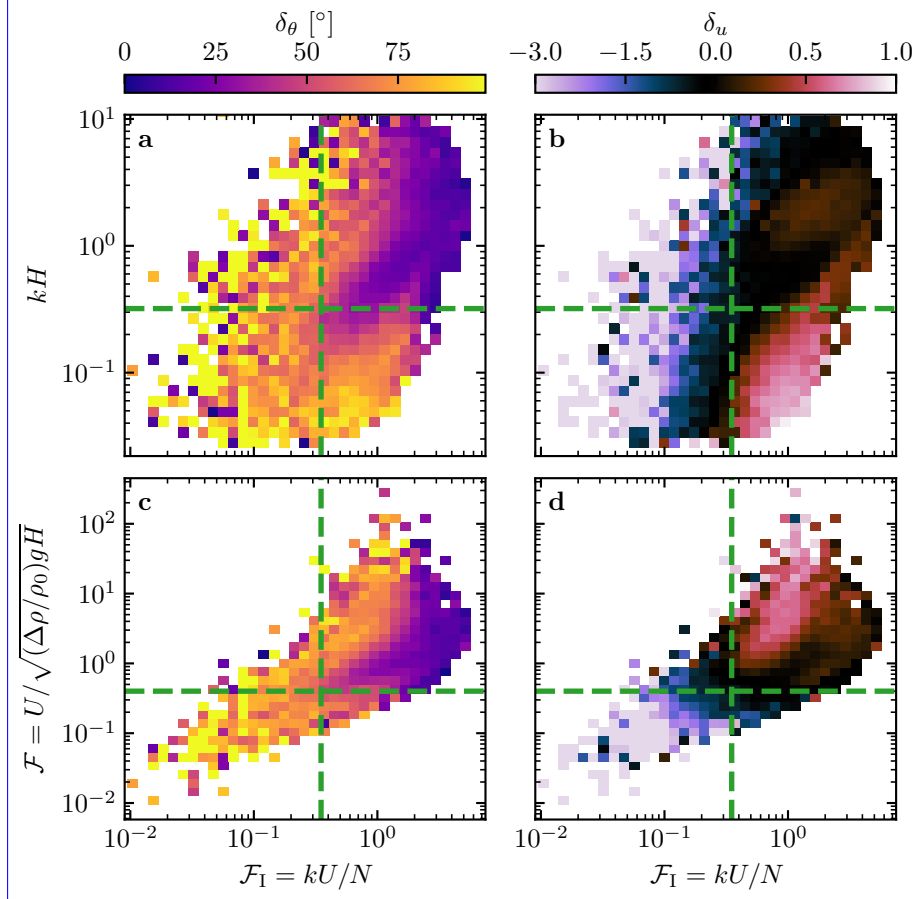


Fig. S11 Regime diagrams of the wind deviation δ_θ and relative attenuation/amplification δ_u in the spaces (\mathcal{F}_I, kH) and $(\mathcal{F}_I, \mathcal{F})$, containing the data from both the North Sand Sea and South Sand Sea stations. Green dashed lines empirically delimit the different regimes. The point density in each bin of the diagrams is shown in Online Resource Fig. S10 – 95% of the data occur in the range $-1 < \delta u < 1$. The similar regime diagrams in the space (\mathcal{F}, kH) are shown in Fig. 8.

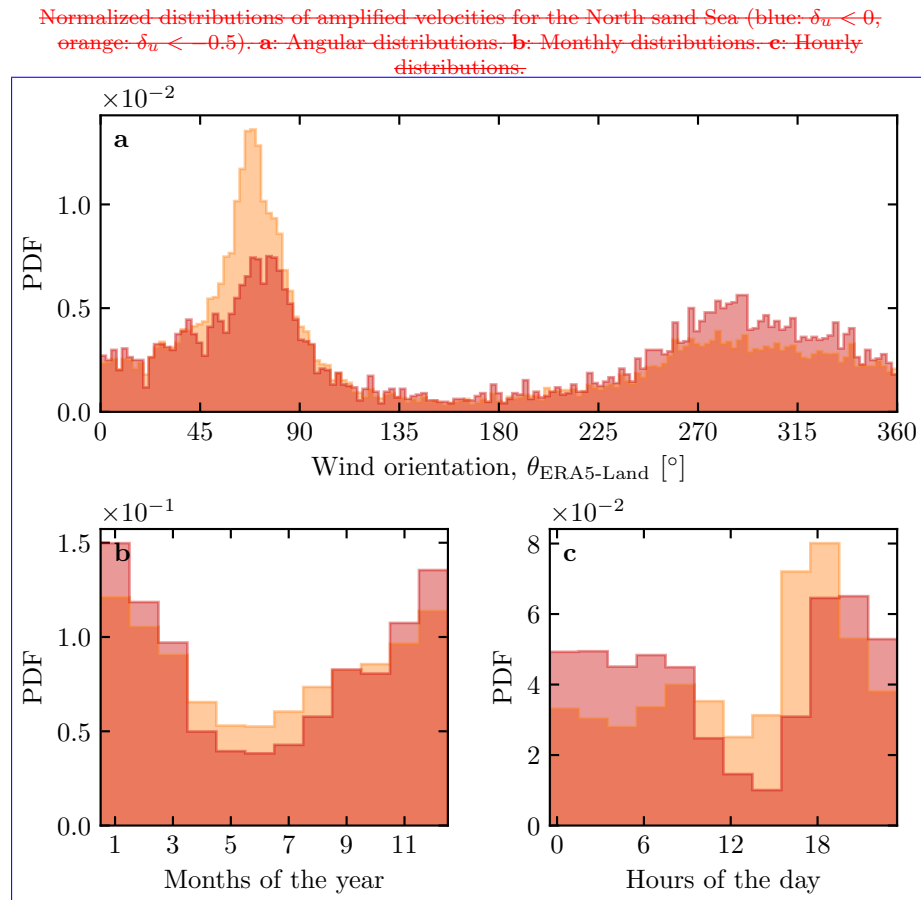


Fig. S12 Normalized distributions of amplified velocities for the North Sea (light orange: $\delta_u < 0$, orange: $\delta_u < -0.5$). **a:** Angular distributions. **b:** Monthly distributions. **c:** Hourly distributions.

Computation of the flow disturbance with the linear model of Andreotti et al. (2009). **a** and **b** Magnitude of the hydrodynamic coefficients A_0 and B_0 , calculated from the values of the non-dimensional numbers corresponding to the ERA5 Land time series presented in Figs. 4 and 5. **c** Shear velocity streamlines over sinusoidal ridges of amplitude $k\xi_0 = 0.1$ and for increasing values of $\sqrt{A_0^2 + B_0^2}$. From the upper to the lower streamline, values of $(kH, \mathcal{F}, \mathcal{F}_I, A_0, B_0, \sqrt{A_0^2 + B_0^2})$ are (1.9, 0.6, 1.5, 3.4, 1.0, 3.5), (1.5, 0.3, 0.4, 4.8, 1.4, 5.0), (0.1, 3.5, 1.0, 8.6, 0.1, 8.6), (0.5, 0.05, 0.04, 9.6, 2.5, 9.9).

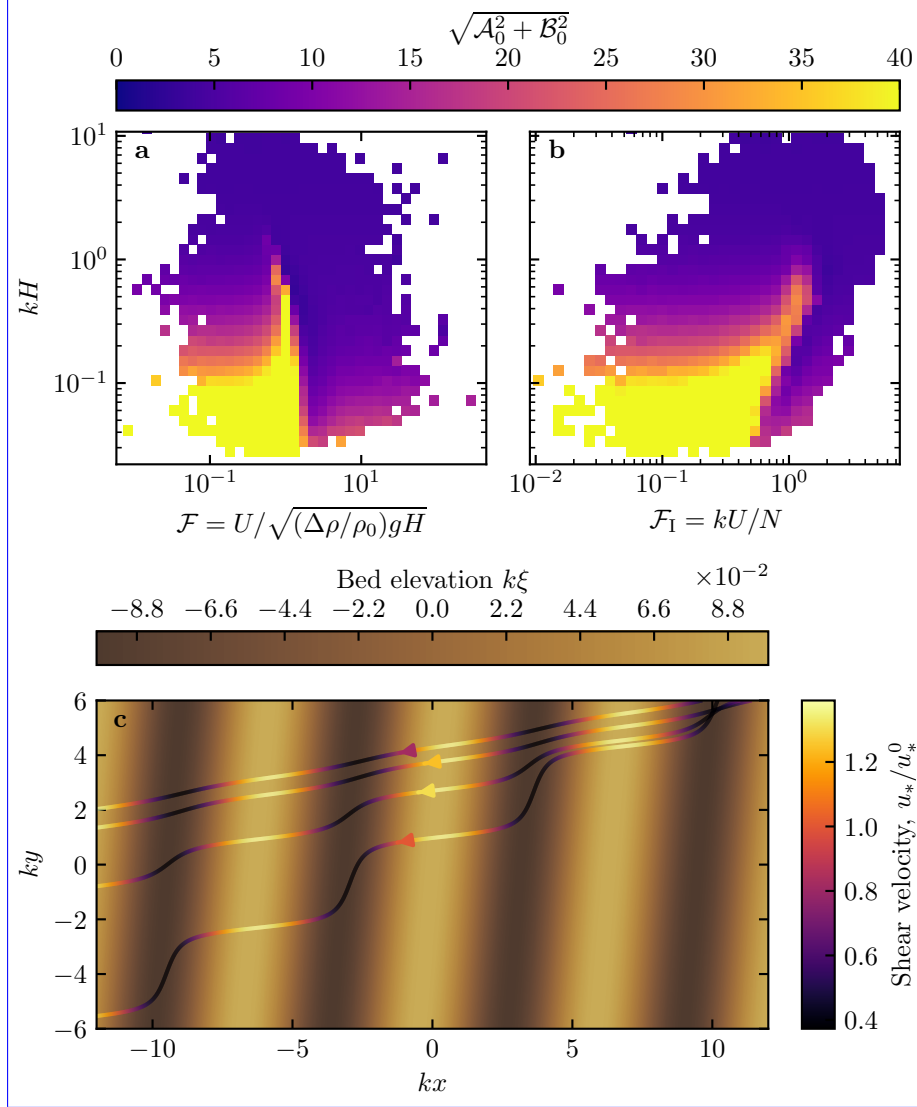


Fig. S13 Computation of the flow disturbance with the linear model of Andreotti et al. (2009). **a–b:** Magnitude of the hydrodynamic coefficients A_0 and B_0 , calculated from the time series of the non-dimensional numbers corresponding to the ERA5-Land wind data and ERA5 data on vertical pressure levels. **c:** Shear velocity streamlines over sinusoidal ridges of amplitude $k\xi_0 = 0.1$ and for increasing values of $\sqrt{A_0^2 + B_0^2}$. From the upper to the lower streamline, values of $(kH, \mathcal{F}, \mathcal{F}_I, A_0, B_0, \sqrt{A_0^2 + B_0^2})$ are (1.9, 0.6, 1.5, 3.4, 1.0, 3.5), (1.5, 0.3, 0.4, 4.8, 1.4, 5.0), (0.1, 3.5, 1.0, 8.6, 0.1, 8.6), (0.5, 0.05, 0.04, 9.6, 2.5, 9.9).

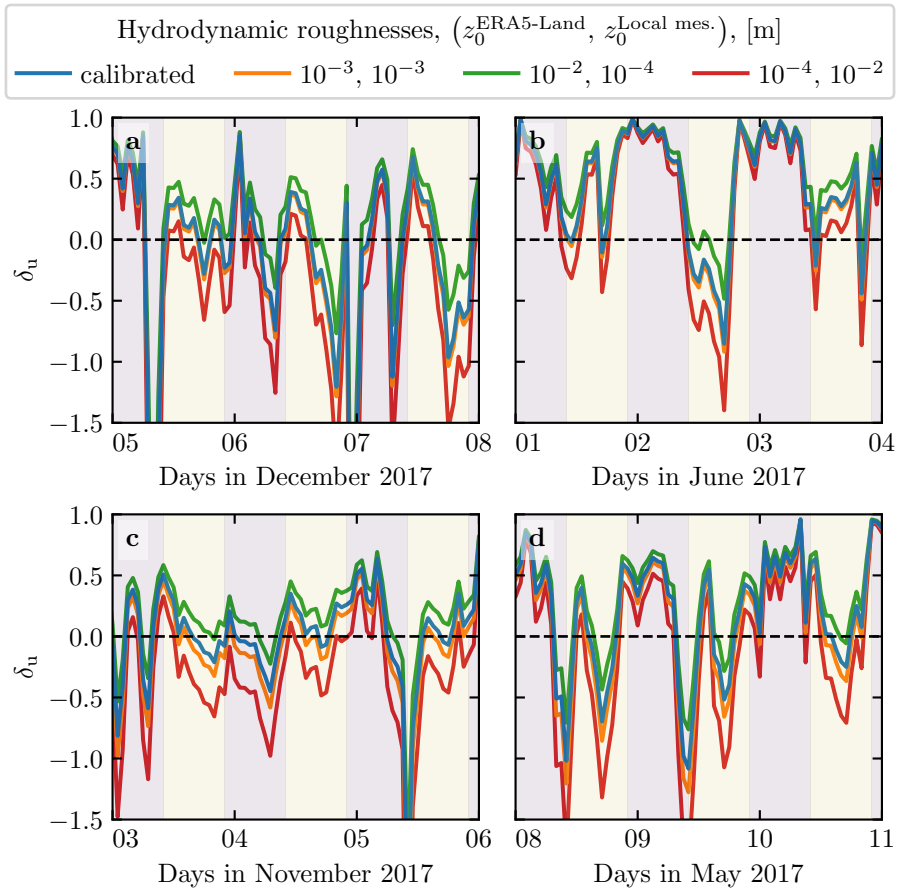


Fig. S14 Time series of the relative velocity disturbance δ_u corresponding to Fig. 5, for different values of the hydrodynamic roughnesses. **a:** North Sand Sea – summer. **b:** North Sand Sea – winter. **c:** South Sand Sea – summer. **d:** South Sand Sea – winter. Note that δ_θ is independent of the choice of $z_0^{\text{ERA5-Land}}$ and $z_0^{\text{Local mes.}}$.